Supplementary Materials for

Fire and grass-bedding construction 200 thousand years ago at Border Cave, South Africa

Lyn Wadley*, Irene Esteban, Paloma de la Peña, Marine Wojcieszak, Dominic Stratford, Sandra Lennox, Francesco d'Errico, Daniela Eugenia Rosso, François Orange, Lucinda Backwell, Christine Sievers

*Corresponding author. Email: lyn.wadley@wits.ac.za

Published 14 August 2020, *Science* **369**, 863 (2020)
DOI: 10.1126/science.abc7239

This PDF file includes:

Materials and Methods

Excavation

Border Cave is situated on a cliff in northern KwaZulu-Natal, on the border of eSwatini (formerly Swaziland) (fig. S1). Background to the area and the new excavations can be found in (*13*). The site has been excavated by a multidisciplinary team since 2015, using standard archaeological methods. The excavation is under the directorship of Dr L. Backwell with permit # SAH 15/7645 from the KwaZulu-Natal heritage agency, Amafa. All excavated material is housed in the Evolutionary Studies Institute, University of the Witwatersrand, which is also the repository for the earliest excavation material by Dart and colleagues.

Border Cave was excavated in 50 cm quadrants numbered by their North and East bearings. Excavation is by natural stratigraphic layers and features within the larger Members of white ash or brown sand recognised during Beaumont's excavations in the 1970s (*15)* and 1980s. Layers are given a colour name from the Munsell Colour Chart followed by an alphabetically arranged name, for example, all names in Member 5 WA (5WA) begin with K, hence the name Dark Brown Kevin (fig. S2), henceforth shortened to 5WA-DBK. The named layers were subdivided as plans when a pavement of lithics formed a discrete floor and/or when features appeared on the sediment surface. Plans, for example, 5WA-DBK Plans 1-3, are minor stratigraphic divisions (*décapages)* with 1 being the youngest and 3 the oldest. All finds larger than 20 mm were plotted in three dimensions using a total station, Nikon Nivo 5C. Piece plotting was either conducted reflectorless or using a prism. The larger than 2 cm items in each layer were mapped with the total station and the numbers provided for individual items, for example, #6299, refer to the number allocated by the total station. Other finds were recovered in nested 1 mm and 2 mm screens. The excavations into Member 5 WA were from squares N109 E113, N108 E113 and N108 E114. These are not full metre squares because they are remnants eroded from Beaumont's 1980s excavation. In Beaumont's grid (*15*) they may be squares P16 and Q16, on the edge of the Horton pit (*13*). Fig. 1 and fig. S17 (site plan and profiles, and plotted lithics) were produced with Inkscape and QGIS Software.

Table S1 presents the dates obtained for Border Cave Members, using radiocarbon dating of charcoal and other plant material, and Electron Spin Resonance (ESR) on tooth enamel. Member 5 WA, the subject of the study here, has dates of 227±11 ky and 183±20 ky ago, based on ESR dating of two teeth. Although these represent the oldest dates obtained for the site, there is an older member, Member 6 BS, under Member 5 WA (fig. S2), for which there is no chronology. Millard's Bayesian modelled dates [see fig. 4 in (*18*)] for the boundaries between all the units were not tabulated. He provided the 95,4% probability ranges (ky ago) for the boundaries of Members 5 BS and 5 WA as follows:

Start of 5 BS / End of 5 WA	155.0	177.0
Start of 5 WA	210.9	797.7

Millard comments that because there were no dates below 5 WA, and only two dating samples from that unit, the start date for 5 WA is imprecise, and probably overestimated (*18*). It does seem, however, that Member 5 WA is older than 200 ky ago.

Micromorphology

Micromorphological samples were collected from horizontal and vertical surfaces of the excavation; some were intended for the collection of plant in the bedding and others for collecting evidence about combustion features (Fig. 4, and figs S3 and S15). Four micromorphological blocks were removed in toto from the exposed plant-rich floor of 5WA-DBK. To do this, cuts were made into the sediment around exposed plant, and the standing blocks were consolidated with jackets made from gypsum bandages (fig. S3). Loose sediment samples were also collected. The three dimensional positions of the blocks were recorded with the total station, and the blocks were photographed before and after excavation. An additional block was cut from the vertical face of the excavation (fig. S3) so that the stratigraphy of the feature could be studied microscopically. This block was later resin-impregnated and thin sections were cut from it (Fig. 4) at the Charles McBurney Laboratory for Geoarchaeology, University of Cambridge, UK. The plant layer is now approximately 20 mm thick, as seen in the thin section, but was probably much thicker in the past, prior to compression. Over time plant layers are compacted through trampling and the weight of overlying sediments (*19, 20*). Loose sediment samples were also collected for Fourier Transform Infrared (FTIR) spectroscopy analyses and phytolith analyses. The original extent of 5 WA bedding is unknown; it was partly excavated by Beaumont (deceased) and the 1987 excavation is unpublished. Thus, we are aware that we have recovered merely a sample of the original bedding feature.

Macroscopic plant identification

Grass fragments and plant specimens were removed from micromorphological blocks using fine tweezers. A Phenom Pure+ Scanning Electron Microscope (SEM) was used for the plant imagery. Metal stubs (26 mm wide) and double-sided tape were used to mount fragments of plant from the micromorphological blocks.

Chemical analyses of grass bedding and ash samples: ATR-FTIR, SEM-EDS, EDXRF and XRD

Samples were extracted from micromorphological blocks (figs S3 and S4) and analysed from the bedding feature 5WA-DBK for their mineralogical composition. In addition, samples were analysed from the ashy layer 5WA-VPBK, which is located underneath the bedding feature 5WA-DBK.

Fourier Transform Infrared (FTIR) spectroscopy was performed with a Bruker Alpha spectrometer set with an Attenuated Total Reflectance (ATR) module equipped with a diamond crystal. The samples were finely ground in a mortar to obtain a homogeneous composition and an optimal contact with the crystal. Spectra were acquired in the mid-IR range between 400 and 4000 cm^{-1} (Deuterated TriGlycine Sulfate detector) with 64 scans and a resolution of 4 cm^{-1}. Background spectra were recorded regularly and the spectra were corrected with an atmospheric compensation using OPUS 7.5 software.

5WA-DBK samples included fragments of putative plant material, plant material mixed with sediment, and sediment within the bedding (fig. S5). Two 5WA-VPBK samples were analysed using ATR-FTIR (fig. S6); a third was analysed (see below) using scanning electron microscopy coupled with energy dispersive X-ray spectroscopy (SEM-EDS), energy dispersive X-ray fluorescence (EDXRF) and X-ray diffraction (XRD) (fig. S7). For comparison, various ashy layers from the younger parts of the sequence were also analysed with ATR-FTIR,

including samples from Member 1 WA (layer Barry), Member 2 WA (white ash top under Member 2 BSL grass bedding), Member 3 WA, Member 4 WA (layer White 3), Member 5 BS (layer Jan) (fig. S8). Other analyses were performed on modern *Panicum maximum* (collected at the entrance of the cave) and its ashes were compared to those from younger grass bedding from Members 2 WA and 2 BSL which were desiccated, not burned (fig. S9; table S2).

For the SEM-EDS analysis, a sediment sample from 5WA-VPBK was placed on a SEM Stub. SEM observations and Energy Dispersive X-Ray spectroscopy (EDS) analyses were conducted with a Tescan Vega3 XMU scanning electron microscope (TESCAN FRANCE, Fuveau, France) equipped with an Oxford X-MaxN 50 EDX detector (Oxford Instruments, Abingdon, U.K.). The sample was observed with no prior metal or carbon coating under low vacuum mode (N2 pressure = 5 Pa). A 10 kV accelerating voltage was used for imaging using secondary and backscattered electrons, and 20 kV for EDS analyses. EDS spectra were processed with the Aztec software (version 3.1, Oxford Instruments).

Additional elemental analyses of sediment from 5WA-VPBK were performed using an Ametek SPECTRO xSORT energy dispersive X-ray fluorescence (EDXRF) spectrometer equipped with a silicon drift detector (SDD), a W X-ray tube with an excitation source of 40 kV, 0.1 mA. One measurement was taken with a spectra acquisition time of 300 s and results were calibrated according to published methodology (*34*). X-ray diffraction (XRD) patterns were collected on a PANalitycal X'pert MPD-PRO Bragg-Brentano θ-θ geometry diffractometer equipped with a secondary monochromator and an X'celerator detector over an angular range of 2θ = 8-80°. The acquisition time was set to 20 hours. The Cu-Kα radiation was generated at 45 KV and 40 mA (lambda = 0.15418 nm). The sample was ground manually and prepared on a silicon wafer sample holder (zero background sample holder) and flattened with a piece of glass. Mineralogical phases were identified by using the Match! Software package (Version 3.8.3.151, Crystal impact, Germany).

Phytolith extraction and classification

Materials

Four sediment samples were analysed in this study. Three samples were collected: from the top, bottom and loose soil of a micromorphological block (BP6357) of the bedding feature 5WA-DBK (fig. S4). One sediment sample was also taken from the ashy layer 5WA-VPBK (ash below the bedding feature 5WA-DBK).

Phytolith extraction

The phytolith extraction from the sediment samples was carried out at the palaeobotanical laboratory of the Evolutionary Studies Institute of the University of the Witwatersrand following the fast extraction procedure of (*35*). The initial sediment weight did not require more than 20 mg due to the phytolith richness of the samples. Carbonate minerals were dissolved adding 50 µl of hydrochloric acid (6 N HCl). After the bubbling ceased, 450 µl of 2.4 g/ml sodium polytungstate solution $Na_6[(H_2W_{12}O_{40})\cdot H_2O]$ was added. The tube was vortexed, sonicated and centrifuged for 5 min at 5000 rpm (Sigma 1-14 microcentrifuge). The supernatant was subsequently removed to a new 0.5 ml centrifuge tube and vortexed. For examination under the optical microscope, an aliquot of 50 µl of the supernatant

was placed on a microscope slide and covered with a 24 x 24 mm cover-slip. Quantification of the phytolith frequency in one gram of sediment was based on 20 fields at 200x magnification whereas morphological identification of phytoliths took place at 400x magnification using an optical microscope (Zeiss).

Phytolith classification

Modern reference collections of South African plants (*36-41)* and modern surface soils (*36, 37, 40*, *42*) were used as comparative material for morphological identification and plant classification. The terminology for describing phytolith morphotypes was based on the anatomical and/or taxonomic origin of the phytoliths. When this was not possible, geometrical traits were followed. Descriptions and naming of the phytoliths follows the International Code for Phytolith Nomenclature (ICPN) 2.0 (*43*).

Charcoal Analysis

Charcoal specimens to be identified were taken from the excavated charcoal from 5WA-DBK by means of random sampling (*44-46*).

The International Association of Wood Anatomists (IAWA) codes from modern wood charcoal of several species listed near Border Cave were recorded from the InsideWood database (*47, 48*) and from published references (*49-51*). Charcoal reference collections are held at the University of the Witwatersrand, Johannesburg (*52-55*).

Charcoal identifications were made using light microscopy, with an Olympus SZX 16 stereomicroscope magnified up to 110x, an Olympus USB camera and soft imaging solutions software. Anatomical details were studied with an Olympus BX51 reflective, polarised light microscope magnified up to 500x and Olympus Stream Essentials image analysis software with Extended Focal Image (EFI) capability.

The woody taxa were identified from charcoal anatomy by matching the IAWA-characteristics according to standard methods (*56-63*). Identification tables were prepared to compare the IAWA numbers with the reference material (*52-54, 64-66*), including finer features and supporting microphotographs, while referring to other studies (*57-61, 63*).

Lithic analysis

The technological classification of the material followed the methodology in (*67*).

Ochre microagglomerate analysis

Five blocks of sediment from 5WA-DBK showing remains of fossilized grass on their surfaces were observed under a Wild M3C reflected light optical microscope coupled with a Nikon Coolpix 990 digital camera. Red, orange, yellow and brown (ROYB) microagglomerates (grains) larger than 150 µm and composed of microparticles lying on the surface of each block were systematically photographed, collected and put on carbon adhesive tabs adhering to SEM stubs. Red, retouched microflakes and identifiable red quartz grains were not collected. For each microagglomerate we recorded contextual (member, layer, square, plan, bucket point), and morphological (shape,

colour, texture, grain size, presence of inclusions) data. Dimensions were then calculated using the ImageJ software (National Institute of Health, University of Winsconsin).

Block 1 was excavated under the microscope on a surface of 6x5 cm. The excavation was conducted in four thin *décapages*. Retrieved sediment was weighed, photographed and observed under the microscope. Red, orange, yellow and brown microagglomerates were systematically collected and counted. Those larger than 150 µm were also photographed and analysed following the procedure described for those collected on the surface. Some microagglomerates larger than 150 µm were kept on SEM stubs and the remainder was kept in plastic sample tubes. Microagglomerates smaller than 150 µm were simply counted and kept in sample tubes. When friable, microagglomerates were disaggregated to access their inner structure when observed with SEM-EDS.

Sediment samples from layers Reddish Grey John, located above 5WA-DBK and 5WA-VPBK and 6BS-Brown Lad located below 5WA-DBK were analysed following the same procedure described for the sediment retrieved from Block 1. We also applied this procedure to a sample of sediment naturally deposited on a 1.10x0.65 m tray, called thereafter 'control sediment', placed inside the cave between 12/03/2016 and 06/04/2017.

Spalls from the control sediment, resulting from roof fall, were observed under the microscope and photographed. Fragments of rock from 5WA-DBK, collected as possible ochre during the sieving process, were also observed under the microscope and photographed.

Two microagglomerates from archaeological layer Reddish Grey John, four from 5WA-DBK, one from 5WA-VPBK, one from Brown Lad, two from the control sample, and one roof spall from the control sample featuring red inclusions were analysed with scanning electron microscopy coupled with SEM-EDS and µ-Raman spectroscopy (µ-RS). The same analytical protocol was applied to one fragment from 5WA-DBK identified as a possible ochre piece in the sieved sediment and a fragment of roof spall from the control sediment featuring red inclusions under optical microscopy. Selected microagglomerates are, as far as possible, representative of the variability recorded when collecting them under optical microscope. SEM observations and EDS analyses were conducted with a Tescan Vega3 XMU scanning electron microscope (TESCAN FRANCE, Fuveau, France) equipped with an Oxford X-MaxN 50 EDX detector (Oxford Instruments, Abingdon, U.K.). Samples were observed with no prior metal or carbon coating. Most samples were observed under secondary vacuum (~5 10-2 Pa). Low vacuum mode (N2 pressure = 5 Pa) was used when necessary. A 10 kV accelerating voltage was used for imaging using secondary and backscattered electrons, and 20 kV for EDS analyses. EDS spectra were processed with Aztec software (version 3.1, Oxford Instruments, UK).

The mineralogical composition of the red microagglomerates was determined by µ-RS using a SENTERRA Dispersive Raman Microscope (Bruker) equipped with an internal calibration system. The working area was examined using an integrated colour camera. Measurements were acquired with a 785 nm laser and a power of 1 mW in order to avoid thermal transformation of mineral phases. The spectra were recorded with an integration time varying from 5 to 10 s, in a spectral range from 100 to 2200 cm^{-1}, and with a number of co-additions varying between 5 to 10 depending on the presence of fluorescence radiation and signal-to-noise ratio. Data were collected and treated with the software package OPUS 7.2 (Bruker, Billerica, USA). Mineral identification was based on the

comparison of the recorded spectra with those of available spectra libraries, such as the RRUFF (*68*) spectra library (University of Arizona).

Supplementary Text

Chemical analyses of grass bedding and ash samples: ATR-FTIR, SEM-EDS, EDXRF and XRD

ATR-FTIR analyses allowed quick identification of the compounds present in the plant and ash layers at Border Cave. The oldest grass bedding from 5WA-DBK, was analysed as well as sediment from ashy layer 5WA-VPBK under 5WA-DBK, grass from younger bedding units, modern grass, *Panicum maximum*, which grows profusely in the area today, and also ash under grass bedding from various members through the sequence.

5WA-DBK grass bedding

The ancient grass spectra from FTIR are documented in fig. S5A. Spectrum A, recorded on putative plant material, is characteristic of amorphous silica with its vibrational band around 794 cm^{-1} (*9, 69*). The bands at 452, 523, 1059 and 1181 cm^{-1} are often found in the spectra of silicate minerals and are related to Si-O bending and stretching modes (*70-72*). Two other bands are observed in the spectrum at 1624 and 3379 cm^{-1} and they respectively correspond to bending and stretching modes of hydroxyl groups of hydrated silica. The IR analysis of white fibrous strands allows their attribution to silicified plant material. Sample B (fig. S5B) comprises sediments associated with some white fibrous material. The single band at 794 cm^{-1} in Spectrum A, attributed to amorphous silica, became a doublet (780 and 795 cm^{-1}) in Spectrum B which, in combination with the appearance of the band at 693 cm^{-1}, shows the presence of quartz (*73*). The other bands in spectrum B are more generally attributed to silicates. Spectrum C (fig. S5C), recorded from some beige sediment within the 5 WA bedding from square N109, E113, shows the presence of quartz, silicates and apatite, with a doublet at 600 and 561 cm^{-1}. Spectrum D recorded on white nodules (fig. S5D) clearly identifies the presence of gypsum with the sulphate vibrations at 456, 597, 667, 1005 and 1102 cm^{-1} (*71*). The bands at 1620, 1683, 3244, 3399 and 3517 cm^{-1} are related to hydration of water and allow it to be distinguished from anhydrite (*71, 74*).

5WA-VPBK

Two spectra were collected from the ashy 5WA-VPBK sediments (BP6405) (fig. S6). Spectrum A, acquired on a bone fragment, records the presence of apatite with the PO_4 phosphate stretching vibrations at 471, 563, 601, 629, 961, 1019, and 1086 cm^{-1}, and the CO_3 stretching vibrations at 875, 1415 and 1456 cm^{-1} and the OH stretching vibrations at 3403 and 3573 cm^{-1}. All these bands show that this is calcined bone that would have been burned at high temperatures.

Spectrum B recorded on loose sediment shows the presence of silicates (450, 782, 797, 1048 and 1078 cm^{-1}), apatite (562 and 598 cm^{-1}) and gypsum (668, 1619, 1681, 3400 and 3507 cm^{-1}).

ATR-FTIR results are consistent with additional chemical analyses conducted on sediments from 5WA-VPBK. EDXRF analyses (table S3) identify the presence of Si (27,9 %), and to a lesser degree, Ca (3,6 %), Fe (1,7 %), K (1,3 %) and Ti (0,1 %). This matches SEM-EDS results (fig. S7, A and B, and table S4) that show the

presence of irregular and angular silicate grains with a length of 66-144 μm identified as quartz (fig. S7C), irregular particles of calcium carbonates (67-186 μm in length) and irregular and angular particles of calcium phosphates with a length of 12-400 μm identified as hydroxyapatite using XRD (fig. S7C). Grass material, irregular barium sulphate particles and sodium chloride identified as halite using XRD (fig. S7C) were also detected. Mineralogical analysis also identified the presence of gypsum and calcite (fig. S7C).

Sediments through the Border Cave sequence (layers younger than 5 WA), and modern Panicum maximum

The sediment sequence at Border Cave was sampled from the eastern profile and analysed by ATR-FTIR spectroscopy. Numerous white layers, intuitively identified in the field as ash, are present, often under bedding layers, but sometimes also on top of them, where presumably the bedding was burned, then not refreshed with clean grass. In Member 4 WA, they form thick layers (several tens of centimetres – fig. S2). The composition of these white layers varies both horizontally and vertically. They most often comprise calcite, apatite, silicates (i.e. quartz and clay) and sometimes gypsum and aragonite. ATR-FTIR spectra obtained on samples from both old and young members (fig. S8) reveal silicates, and sometimes also quartz bands; these mainly come from the disintegration of cave roof material. Calcite was identified in almost all white layers and its main origin is probably wood-ash. Aragonite was a rare inclusion in the white sediments and one likely source is giant land-snail shells that have been recovered occasionally at the site; another likely source is burning of grass (see below). Gypsum is also rare in the white layers; it occurs in isolated patches and may have its origin from weathering of roof material, from transformation of ashes, or from the breakdown of organic matter. Apatite vibrational bands are present in most of the white layer samples analysed. The inclusion of apatite can be due to three main factors at Border Cave: the presence of bone, the diagenetic alteration of calcite as a component of plant ash, especially from certain grass types like *Panicum maximum* (*24*) (fig. S9C), and also from guano. Many bone fragments are present in the white ash. When the IR spectrum exhibits a band around 630 cm^{-1}, the apatite is mainly due to calcined bone; this band shows a recrystallisation process of bone hydroxyapatite through heating (fig. S8, A and D).

Figure S9 presents ATR-FTIR results for *Panicum maximum:* the spectra obtained on fresh and dried *Panicum maximum* (fig. S9, A and B), and its ashes (fig. S9C). Non-silicified bedding layers from Members 2 WA and 2 BSL have spectra recorded in fig. S9, D and E, respectively. The spectra of fresh and dried *Panicum maximum* are similar and show the characteristic bands of cellulose; shifts of some bands appear after drying (fig. S9, A and B). While grass pieces can be seen inside the layers 2 WA grass bedding Dossy, and 2 BSL grass bedding, the FTIR spectra show that their initial composition underwent degradation (fig. S9, D and E). The bands around 2850 and 2919 cm^{-1} illustrate that some organic matter is still present in the form of C-H bonds but the structure is now amorphous; this is shown by the wide bands around 1393 and 1592 cm^{-1} which are characteristic of amorphous carbon. The spectrum of *Panicum maximum* ashes shows the presence of calcite (873 and 1402 cm^{-1}), aragonite (701, 865 and 1469 cm^{-1}), amorphous silica (781 cm^{-1}) and other silicate bands (420, 432, 666, 831, and 1009 cm^{-1}), apatite (569 cm^{-1}) and potassium sulphate (619, 1114 cm^{-1}; fig. S9C). The amorphous silica is due to the presence of phytoliths. The presence of aragonite suggests that the temperature generated by the grass burning (possibly

smouldering) was below 400 or 500°C, the temperature at which aragonite transforms into calcite (*75*). Aragonite detection in the BC sediments can then be due to the burning of grass, in addition to the presence of snail shells.

Phytolith analysis

Phytolith concentration and preservation

Table S5 lists the phytolith concentration (phytoliths per gram of sediment), the total number of phytoliths counted per sample, and the percentage of epidermal phytoliths articulated anatomically. Phytoliths were identified in the three 5WA-DBK samples in very high concentrations. The sediment samples collected from the top and bottom of the micromorphological sample (BP6357) contained the highest frequencies of phytoliths per gram of sediment, 92,1 and 107,2 million, respectively. Only two diatoms (bio-siliceous microfossils) were detected in the top sample. Charred remains of the epidermis (cuticles) of grasses were also recovered in relatively high frequencies. The samples analysed from the ashy compacted sediments from 5WA-VPBK also showed very high phytolith concentration, making up to 70,5 million phytoliths per gram of sediment.

Taphonomy

Phytoliths with signs of weathering were minimal and therefore not considered in this study. We consider the percentage of articulated phytoliths and, following (*76*), the average number of cells per anatomically connected cells as indicators of physical breakage and therefore of preservation (table S5). Between 62,3 and 57,2 % of the phytoliths counted per sample from 5WA-DBK formed part of interconnected cell structures (table S5). The average number of cells per the total number of phytoliths in anatomical connection was 6,1 and 4,6 in the top and bottom of the micromorphological sample, respectively, and 5,2 in the loose sediment sample collected around the micromorphological sample. 5WA-VPBK also revealed high frequencies of articulated phytoliths, comprising 64,3 % of the phytoliths counted; the average number of articulated cells is 5,2 (table S5).

Phytolith morphology

A total of 77 phytolith morphotypes was identified (table S6), and these were later grouped in 14 general categories: grass phytoliths (epidermal GRASS SILICA SHORT CELLS-GSSCP, ELONGATES with decorated sides and ELONGATES PAPILLATE), ELONGATES ENTIRE (without decorated sides), ACUTE BULBOUS (including trichomes and prickles), PAPILLATE, mesophyll, SCLEREIDS, STOMATA, TRACHEARY, dicot silicified epidermis, BLOCKY morphologies (all types), SPHEROIDS and unidentified phytoliths (fig. S10).

The phytolith assemblage was very diverse, as indicated by the high phytolith morphological variety (table S6). Phytolith morphotypes characteristic and diagnostic of the Poaceae family represented between 77-64 % of the total phytolith assemblage (fig. S10). Among grasses, ELONGATES with decorated sides (mainly ELONGATES COLUMELLATE, LIGULATE and SINUATE) were most common (figs S10 and S11, A to C). Multi-papillate epidermal long cells with columellate/ligulate and sinuate decorated sides were also common (figs S10 and S11, D to F; table S6). GSSCP BILOBATES were also very abundant and were the most common GSSCPs identified in samples,

accounting for 91-71 % of the total GSSCPs (figs S11, G to I, and S12). Trichomes and prickles (ACUTE BULBOUS), which probably belong to grasses, were also identified in high frequencies (fig. S11C, table S6).

Articulated phytoliths from the leaf epidermis of dicotyledonous plants were also identified in the three samples with the highest frequencies found in the sediments collected from the top of the micromorphological sample (fig. S11, J to L). The sample from 5WA-VPBK had these morphotypes, too, but in low frequencies.

Comment on phytolith results

The phytolith concentration detected in the studied samples (from 5WA-DBK and 5WA-VPBK) was highly anomalous. Therefore, we compared our material to other published phytolith studies that used the same or similar quantitative approaches (*35, 77, 78*) (table S7). Most of the phytolith studies that used Albert's method (*77, 78*) published the phytolith concentration based on the total Acid Insoluble Fraction (AIF). The difference between the total concentration based on AIF or initial amount of sediment (in grams) does not vary considerably (*35*), and therefore we also considered those studies for comparison.

To the best of our knowledge, the highest phytolith concentration so far found in the literature comes from a room belonging to a large residential building of the Israeli Iron Age site of Tel Dor (46 million phytoliths per gram of sediment) (*79*) (table S7). Dahllite was the main mineral component identified in the sample, but the authors could not find a parsimonious explanation for the activity performed in this space. The second highest phytolith concentration comes from a combustion feature in the Middle Palaeolithic deposits of the Greek Theopetra site (43 million phytoliths per gram of acid insoluble fraction) (*80*) (table S7). At Border Cave, the samples from the top and bottom of the micromorphological block from 5WA-DBK and the sample from 5WA-VPBK are double that from the other sites. This exceptionally high phytolith concentration is interpreted as evidence of the intentional and intensive, and probably continuous accumulation of plants during this occupation level. We suggest that this high plant accumulation is evidence for the presence of a living floor, where bedding was constructed by past inhabitants for their day to day activities.

From a taphonomic perspective, our results are indicative of a good state of preservation of the phytolith assemblage from the bedding feature 5WA-DBK as indicated by the high phytolith concentration and the high percentage of articulated phytoliths identified (62,3 to 57,2 %). The perfectly preserved grass leaf structures showing the upper epidermis and the palisade mesophyll, and the remnants of the putative spongy mesophyll also demonstrate the excellent phytolith preservation in samples (fig. S13).

The bedding at Border Cave comprised a variety of grasses (Poaceae), as evidenced by the various phytolith morphotypes belonging to this family. The excellent phytolith preservation conditions created an opportunity for taxonomic phytolith identification. We compared fossil epidermal grass phytoliths and extant South African grasses from KwaZulu-Natal (*39*) and the Cape south coast (*81*). We observed that the epidermal multi-papillate and non-papillate long cells with columellate/ligulate and sinuate sides identified in our samples resemble those identified in Panicoideae species of *Melinis repens*, *Setaria pallide-fusca* and *Panicum maximum* (*39*), and *Themeda triandra, Setaria sphacelata, Heteropogon contortus* and *Panicum deustum* (*38, 81*) (fig. S14). The comparison of fossil and extant grass epidermal structures reveals that the epidermal multi-papillate and non-

papillate long cells with columellate/ligulate and sinuate sides identified in our samples, and which dominate the phytolith assemblage, can tentatively be identified to five genera of the Panicoideae subfamily: *Heteropogon, Melinis*, *Panicum, Setaria* and/or *Themeda*. The dominance of short cell bilobates supports the association of the grass epidermal phytoliths to grasses from the Panicoideae subfamily. These grasses are widely distributed in South Africa, mainly in the Savanna and Grassland biomes, and are present nowadays in the Border Cave region. Most of these species occur naturally in open woodlands and bushveld vegetation, and grow well in shaded and moist areas, also along rivers.

The presence of charred grass fragments both at the top and bottom of the bedding, as identified during the phytolith analysis, suggests that the bedding was burned for site maintenance before being replaced with fresh grass.

The highest frequency of dicotyledonous plant leaves in the sediment samples comes from the top of the bedding. It is feasible that these dicotyledonous plant remains were the result of plant processing activities such as creating wooden tools, however, their prominent occurrence at the top of the bedding can be interpreted taphonomically and/or behaviourally. Taphonomically, the concentration of dicotyledonous leaves could imply that this layer is the last stage of use of the bedding. This might suggest that at Border Cave, ~200 ky ago, behaviour similar to that at Sibudu (*9*) took place when bedding was constructed, that is, that leaves from trees and shrubs were placed on monocotyledonous bedding.

The high phytolith concentration (70,5 million phytoliths per gram of sediment) present in the ashy 5WA-VPBK sediment demonstrates the elevated representation of plant material, comprising Panicoideae grasses (86,8 %). The state of preservation of the phytolith assemblage in these deposits is excellent, as indicated by the high number of articulated phytoliths (64,3 %; table S5). We interpret these deposits as representing an old living floor (perhaps old bedding) formed by the intentional and intensive accumulation of grasses.

Charcoal identification results

The woody taxa identified from charcoal fragments in 5WA-DBK are listed in table S8.

Of particular interest are two species, *Tarchonanthus trilobus* and *Cryptocarya liebertiana*. Both have aromatic leaves (*21, 82*) and potentially they could have been used on top of the grass bedding for insect repellent purposes as was the case for *Cryptocarya woodii* at Sibudu at 77 ky ago (*9*).

Micromorphological study

Microfacies in 5WA-DBK

Fig. 4, C and D, and fig. S15, A to D, show stratigraphic sequences of microfacies in 5WA-DBK, including homogeneous anthropogenic components (HAC) that include ash lenses (As in Fig. 4, C and D; As-1 and As-2 in fig. S15, A to C; As-3 in fig. S15D) and laminar sediments rich in burnt organic material (LO). Homogeneous anthropogenic components (HAC): This resembles Goldberg's microfacies type 5 described for Sibudu (*22*), but with minor stratification at its upper contact and higher particle abundance than in Goldberg's sample SS-5A-D (*22*). The Border Cave unit is composed of charcoal, burnt bone, partially burnt woody and fibrous organic matter, rubified coarse particles, aggregated particles, quartz particles and rhyolite clasts. The coarse/fine related

distribution pattern is close to single-spaced porphyric, and the unit is generally poorly sorted with some banded distributions of larger particles. Coarse fraction particles are generally poorly sorted and tabular to blocky in shape, while anthropogenic components are sub-rounded to rounded with undulating to smooth surfaces. Particles show isotropic organization in the centre of the unit becoming more planar at the upper contact with the overlying yellow ash microfacies (As-2; fig. S15, A to C). In situ fragmentation is limited to the upper contact. This unit may have been raked, albeit gently, then trampled and compressed. It is in this unit that we find several interstratified layers of bedding (see Fig. 4, C and D, and fig. S15A, features 1 and 2, and fig. S15, D and E) characterized by laterally extensive, articulated, stacked phytoliths and silicified fibrous plant matter. In each case, these strata are found within 1 cm of distinct ash layers (As) overlain by partially burnt bedding (Laminar Organic [LO]). In the bedding layer identified in feature 1 (fig. S15A), the layer thickens towards the centre of the slide and is locally deformed by compression. Slightly higher clay abundance found immediately above feature 1 (fig. S15A), suggests vertical movement and accumulation of clays onto a less permeable, interstratifying layer of vegetation.

Laminar organic (LO): As in Goldberg's microfacies type 2 and 2a from Sibudu (*22*), this dark brown laminar unit is rich in organic matter comprising poorly sorted burnt fibrous and woody organic stringers in varying states of fragmentation, some compressed in situ. Small, rounded rubified sediment particles and aggregates appear sporadically. This facies is dominated by densely packed organic remains, and has a generally close to single-spaced porphyric coarse/fine related distribution pattern. Coarse fraction particles are poorly sorted, generally tabular-planar in shape, subangular to subrounded with rough to undulating edges. Three LO units are present in the two 5WA-DBK thin section samples. In fig. S15, A to C, two subunits within LO-2 are present. The lower subunit is charcoal-poor with a single to double-spaced porphyric related distribution pattern and a generally well-sorted, small coarse fraction. The subunit is rich in phytoliths and burnt bone fragments, has a slightly more chaotic structure than the overlying subunit, but is still roughly stratified. The overlying subunit is charcoal-rich with a close to single-spaced porphyric coarse/fine related distribution pattern and poorly sorted coarse fraction. Coarse particles are mostly subrounded to rounded tabular shapes with some blocky charcoal pieces and particles show well-developed planar stratification. LO-1, in fig. S15A, has a sharp lower contact with an ash microfacies (As-1). The basal layers of LO-1 unit comprise burnt and unburnt elongated, conformably stacked, fibrous and woody elements representing in situ partially burnt bedding. This unit grades upwards into another HAC microfacies in which we find remnant, ephemeral, but distinct interstratifying layers of bedding (fig. S15A, features 1 and 2). Compression-related fragmentation and deformation is present in the upper contacts of all LO units. All LO microfacies units in Fig. 4, C and D, and fig. S15, A to D are interpreted here as burnt and partially burnt compressed bedding.

Phosphatic, phytolith-rich ash (As): As (Fig. 4, C and D; As-3 in fig. S15D), As-1, As-2 (fig. S15, A to C) represent different units, and are equivalent to microfacies type 5 identified in unit 2 of Goldberg's Sibudu sample SS-5A-D (*22*). All units are dominated by fine groundmass (lacking sand-sized quartz grains), have open porphyric coarse/fine related distribution patterns and are rich in phytoliths. Occasional blocky, woody charcoal, ashy aggregates, silicified plant remains, rounded aggregates (some rubified) and fragmented burnt bone (some fragmentation occurring in situ; feature 5 in fig. S15D) are randomly distributed and isolated through the units. As-2 (fig. S15, A to C) shows a slightly higher clay content in various isolated forms, from rough-edged, rounded

nodules, and dispersed, diffuse masses (not filling voids), to short, dispersed, isolated lenses with impressed particles causing localised deformation from above; suggestive of deflation and compression. In As-2, clays line clasts more abundantly at the upper contact, and clay is generally more abundant at the base of the overlying LO-2 unit. No internal stratification is clear, although articulated phytoliths and silicified plant remains in microfacies As-1 are stacked and parallel in orientation, potentially suggesting in situ compression through volume reduction (*19*). Particles are equant to tabular in shape and subangular to rounded with a combination of surface textures from rough (isolated charcoal) to smooth. Particles appear to 'float' within the massive matrix. We interpret these units as ash-rich phosphatic layers formed through disturbances including rake-out, trampling and compression that caused reduction in sediment volume (*19*, *22*).

Stratigraphic contacts

From bottom to top, HAC to As-1 (fig. S15, A to C): The contact between HAC and As-2 is locally irregular and gradational with reworking of underlying sediments into the lower extent of the As-2 unit. The upper contact of As-2 with LO-2 is slightly irregular with localised erosion and deformation, associated with compression and related fragmentation of organic remains. A slightly higher abundance of coarser particles, and an enrichment of clay at the base of the overlying LO-2, suggest a partial consolidation of As-2 and potential settling of larger particles during the first accumulation of LO-2 and further vertical movement of clays onto a slightly consolidated As-2 surface. The contact between the LO-2 subunits is sharp and conformable. The lower contact of ashy unit As-1 with LO-2 has a similar contact to that seen between As-2 and HAC, yet in this case larger aggregated clasts of the underlying LO-2 unit are dislodged. Unit As-1 is overlain by LO-1 and the contact is gradational in the left exposure in the thin section (fig. S15A), sharp in the upper right corner and truncated in the centre of the slide by localised post-depositional mixing. As is the case with the As-2 LO-2 contact, larger particles and clays are more abundant at the lower contact of LO-1. LO-1 (fig. S15A) grades into the uppermost HAC microfacies containing laminar bedding layers (features 1 and 2).

The alternating sequence of these units suggests repeated use of this part of the cave for similar purposes. The silicified bedding material shown in Fig. 4, E and F (also fig. S15E), is located 5 mm above a sequence containing laminar sediments rich in burnt bedding (LO), phosphatic ash rake-out (As) and homogeneous anthropogenic component facies (HAC) in Fig. 4, C and D, and fig. S15D.

Lithic Analysis

The rocks knapped in the bedding of 5WA-DBK were: quartzite, hornfels, rhyolite and basalt (table S9). Agate was also knapped, but this mineral is represented only among the debris (table S10). The main technological categories indicate that there was flake as well as blade/bladelet production. The sample size is too small to recognize whether the two types of blanks are related or are the by-products of two independent reduction sequences. Two triangular blanks and a retouched piece were also retrieved in this assemblage (fig. S16). One refit shows the spatial integrity of the bedding feature (fig. S16). Plotting of the lithics with a total station demonstrates that lithic knapping took place in and around the bedding (fig. S17).

Ochre microagglomerate analysis

Microscopic and morphometric analysis

Red, orange, yellow and brown microagglomerates are more abundant in 5WA-DBK than in the adjacent archaeological layers and the control sediment (table S11). The top of this layer (*décapage* 1), in which the plant remains are the most abundant, features a concentration of microagglomerates per gram that is between twelve and thirty-seven times higher than that observed in over- and underlying layers. It is also much higher than the proportion observed in the control sediment. Particles from 5WA-DBK (fig. S18) also differ from those from the other layers and from the control sample in size, morphology and colour. Particles smaller than 150 μm are substantially more abundant in 5WA-DBK and those larger than 150 μm feature a larger size range than in the other analysed contexts (fig. S19 and table S12). 5WA-DBK is characterized by rounded and, to a lesser extent, irregular particles that are mostly orange and red (table S13). This trend is not observed in the other analysed samples and it is noteworthy that the particles collected in the control sediment are exclusively dark red and mostly angular. Roof spalls are characterized by a hard calcareous matrix containing quartz grains of different sizes. Some of the spalls feature red and brown inclusions reminiscent in colour, shape and size of dark red and brown microagglomerates present in the archaeological layers. Thirty-one fragments were identified as possible ochre during the sediment sieving. They consist mostly of angular clasts of hard ferruginous siltstone that may represent roof spall exposed to heating.

Textural, elemental and mineralogical analysis

Summarised results of the elemental and mineralogical composition of the microagglomerates and fragments from the archaeological layers and the control sample are provided in tables S14 to S17 and figs S19 to S22. Below we present detailed results of the SEM-EDS and μ-RS analysis of the microagglomerates, spall and putative ochre piece.

Detailed results of microagglomerate study by layer

Layer Reddish Grey John

Sample 43 (figs S20A, S21A and S22A) is a rounded agglomerate of red and, more rarely, black grains. SEM-EDS analyses identify the agglomerate as comprising silicate grains interpreted as quartz, although this mineral was not formally detected by μ-RS. The sample also features sub-micrometric iron-rich grains, identified as hematite, but also goethite. Calcium carbonates, sodium chloride and gypsum were also detected.

Sample 44 (figs S20A, S21A and S22A) is an agglomerate of orange and, to a lesser extent, translucent, white, grey, and black grains. SEM-EDS analyses identify a matrix of submicrometric grains rich in Si, Al and Fe, interpreted as iron oxides and clay minerals. This is confirmed by μ-RS, which detected hematite, goethite and kaolinite, large grains (180-190 μm) of calcium sulphates (gypsum) and, less frequently, small silicate grains (15-18 μm) interpreted as quartz. Particles rich in iron and chrome (5 μm) were detected. Sodium chloride and calcium phosphate were also identified.

5WA-DBK

Sample 3 (figs S20A, S21A and S22A) is a rounded agglomerate of dark red and some translucent grains. Elemental and mineralogical analyses indicate this sample mainly comprises large (6-45 μm) homogeneous silicate grains (quartz) surrounded by smaller (1-3 μm) sub-circular and irregularly-shaped quartz grains. Particles of feldspar (45 μm) identified as albite and small (10 μm) angular particles composed of Fe and Ti were also detected. They are surrounded by agglomerates of sub-micrometric particles and platelets rich in Si, Al, K and Fe, interpreted as clay minerals and iron oxides, identified by μ-RS as kaolinite and hematite/goethite respectively. Calcium phosphate and sodium chloride were also detected.

Sample 7 (figs S20, D to E, and S21, D to E) is a rounded agglomerate of orange and few black grains. SEM-EDS identifies irregular silicate particles (12-20 μm) of quartz, angular particles (12 μm) of a mica identified as muscovite, and few grains rich in Fe and Ti, recognised as magnetite and possibly rutile. The matrix is composed of agglomerates of sub-micrometric grains, mostly composed of Fe, Si, Al and K, interpreted as clay minerals, hematite and goethite. Manganite was also detected by μ-RS. Sodium chloride was also detected.

Sample 10 (figs S20, G to H, S21, G to H, and S22E) is an angular agglomerate of orange, and a few black grains, mostly composed of silica, probably quartz. SEM-EDS shows the presence of platy grains of mica (17 μm) identified as muscovite, angular iron oxide particles (4 μm) and irregularly shaped grains rich in Fe and Ti (6-10 μm). They were identified as hematite, magnetite and rutile. These minerals are embedded in a matrix composed of agglomerates of sub-micrometric platelets rich in Si, Al and K, recognised as kaolinite.

Sample 28 (figs S20F, S21F and S22F) is an angular agglomerate of red, and a few black and grey grains. Results of elemental and mineralogical analyses indicate that this sample mostly consists of a large quartz grain surrounded by angular and irregular smaller silicate grains (11-30 μm in length), also identified as quartz, and rare angular iron and titanium-rich grains (140 μm in length). Both are cemented by a matrix comprising rich sub-micrometric particles of hematite and goethite and possibly aluminosilicates such as clay minerals. SEM-EDS additionally identified fragments of vegetal fibres. Sodium chloride was also detected.

5WA-VPBK

Sample 38 (figs S20I, S21I and S22G) is a rounded agglomerate of red, and a few white and black grains. SEM-EDS and μ-RS show that this sample is mainly composed of quartz grains of variable size, from small angular (4 μm) to large angular and irregular (16-170 μm in length). These grains are associated with platy particles (~7 μm) interpreted as K-rich micas. μ-RS also identified the presence of feldspars (albite). The matrix that cements these grains is composed of submicrometric particles of hematite and agglomerates of sub-micrometric potassium and aluminium-rich particles interpreted as clay minerals. Elemental analyses identified the presence of calcium phosphates recognised as fluorapatite, possibly a contamination from the surrounding sediment. Mineralogical analyses also showed the presence of calcite and gypsum.

Layer Brown Lad

Sample 42 (figs S20J, S21J and S22H) is a rounded agglomerate of red-orange, and a few small, black grains. SEM-EDS and μ-RS identified large quantities of quartz grains (~4-12 μm), associated with irregular grains rich in potassium, aluminium and sodium (~28 μm in length), and interpreted as feldspars. This is consistent with the detection of albite. Agglomerates of submicrometric iron-rich grains, characterized as hematite, and submicrometric grains rich in aluminium, iron and potassium, interpreted as clay minerals were also detected. Calcium phosphate was also detected.

Control sediment sample

Sample 39 (figs S20K, S21K and S22I) is a rounded agglomerate of dark red and, to a lesser extent, black and translucent grains. SEM-EDS and μ-RS indicate that this sample consists of a large quartz grain surrounded by smaller angular and irregular (~6-55 μm) quartz grains. These grains are coated by a matrix of submicrometric iron-rich particles (hematite and goethite) and aluminosilicates. A few undetermined platy grains rich in iron and chrome (~6 μm), and platy particles (~9 μm) similar to those identified on samples 40 and 44 (interpreted as mica) were also detected. Other compounds such as carbonates, calcium sulphates, calcium phosphates, and sodium chloride were also identified. An irregular grain of sodium chloride, comparable in morphology with that identified on sample 28 and sample 40 was also observed.

Sample 40 (figs S20L, S21L and S22J) is a rounded agglomerate of dark red, and a few translucent grains. SEM-EDS and μ-RS indicate that it is a compact agglomerate of silicates, characterized as quartz. Platy particles rich in iron and chrome (~5 μm) comparable to those identified on sample 39 and 44, were detected, as well as submicrometric agglomerates of hematite and goethite. Calcium carbonates and sodium chloride grains, showing the same morphology as those identified in samples 28 and 39, were identified.

Possible ochre fragment from 5WA-DBK

SEM-EDS and μ-RS analyses of this dark fragment of a possible ochre piece (OF1) (figs S20M, S21M and S22K) show it is mostly composed of large quartz grains. The matrix consists of a mixture of submicrometric grains rich in Si, Fe, Al, K identified as goethite, hematite and aluminosilicates, possibly clay minerals. Rare-earth elements (La, Ce, Nd) absent in the other analysed samples were detected. Additionally, acicular particles of barium sulphates (~16 μm), platy particles rich in silicon and potassium (~114 μm), and angular particles of silicates rich in Zr (~56 μm) were also identified. An irregular coating of calcium phosphates and sodium chloride was also identified.

Roof spall

The surface of this fragment (figs S20, N to O, S21, N to O, and S22L) features 200-300 μm wide micropits whose walls are coated with red particles. Although made difficult by their morphology SEM-EDS analysis of the pits detected the presence of iron and μ-RS identified the particles coating the pits' walls as mostly comprising hematite and more rarely goethite. Calcium phosphate and sodium chloride were detected on the surface of the roof spall.

Acknowledgements

L.B. directs the Border Cave excavations under permit SAH 15/7645 issued by the KwaZulu-Natal Heritage Agency Amafa. P.d.l.P. conducted lithic plotting for fig. S17. To enable the ochre microagglomerate study, Amafa also issued a permit (SAH19/14032) to L.W. for the export to France (to D.E.R. and F.d'E.) of three sediment samples and one sample of cave roof spall. The CCMA electron microscopy equipment was funded by the Région Sud - Provence-Alpes-Côte d'Azur, the Conseil Départemental des Alpes Maritimes and the GIS-IBiSA. L.W. and C.S. thank SANBI, Pretoria for the use of the Phenom Pure SEM and Dr J. van Rooy for kind assistance. We thank A. Millard for providing the numbers from Fig. 4 in his 2006 paper. B. O. Vilane is thanked for her invaluable help at Border Cave. I.E. acknowledges the DSI-NRF Centre of Excellence in Palaeosciences. F.d'E. and D.E.R thank Eric Lebraud (ICMCB, UMR-CNRS 5026, Université de Bordeaux) and Michel Dubar (CEPAM UMR 7264 CNRS-UNS, Université Côte d'Azur) for their assistance with XRD analyses and Alain Queffelec (PACEA UMR-CNRS 5199 Université de Bordeaux) for performing the XRF analyses. D.S. thanks the Charles McBurney Laboratory for Geoarchaeology, University of Cambridge, UK, for the thin sections of the 5WA-DBK micromorphology block. D.S. was funded by an NRF Research Development Grant for Y-Rated Researchers (Grant number 116358).

Fig. S1.
Position of Border Cave on the border of South Africa and eSwatini (formerly Swaziland).

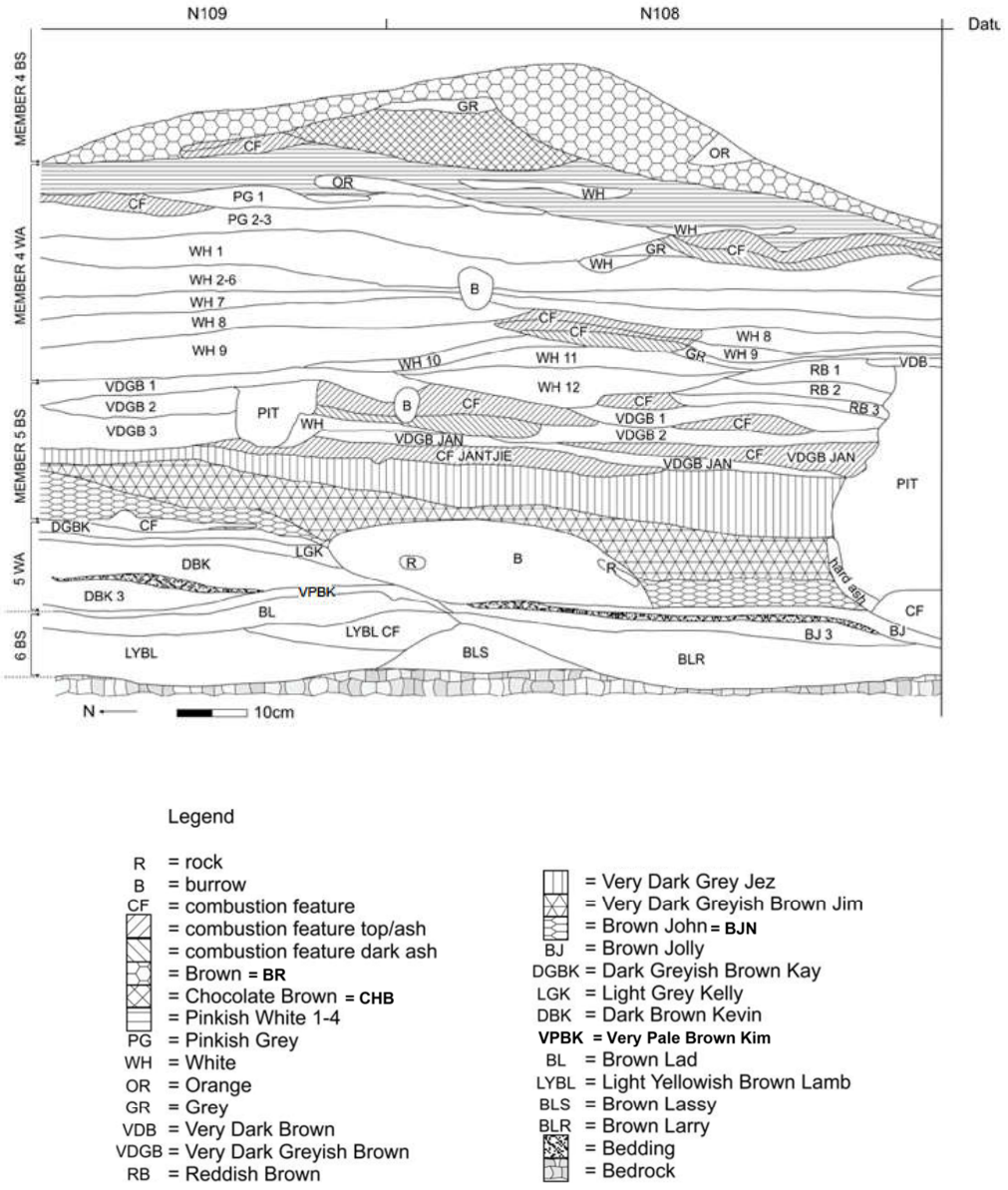

Legend

R = rock
B = burrow
CF = combustion feature
= combustion feature top/ash
= combustion feature dark ash
= Brown = **BR**
= Chocolate Brown = **CHB**
= Pinkish White 1-4
PG = Pinkish Grey
WH = White
OR = Orange
GR = Grey
VDB = Very Dark Brown
VDGB = Very Dark Greyish Brown
RB = Reddish Brown

= Very Dark Grey Jez
= Very Dark Greyish Brown Jim
= Brown John = **BJN**
BJ = Brown Jolly
DGBK = Dark Greyish Brown Kay
LGK = Light Grey Kelly
DBK = Dark Brown Kevin
VPBK = Very Pale Brown Kim
BL = Brown Lad
LYBL = Light Yellowish Brown Lamb
BLS = Brown Lassy
BLR = Brown Larry
= Bedding
= Bedrock

Fig. S2.

Border Cave East profile of Squares N109 E113 and N108 E113 from Member 4 BS to 6 BS. The sediments above Member 4 BS were excavated by Beaumont and were subsequently eroded. See (*13*) for profiles of members younger than 4 BS.

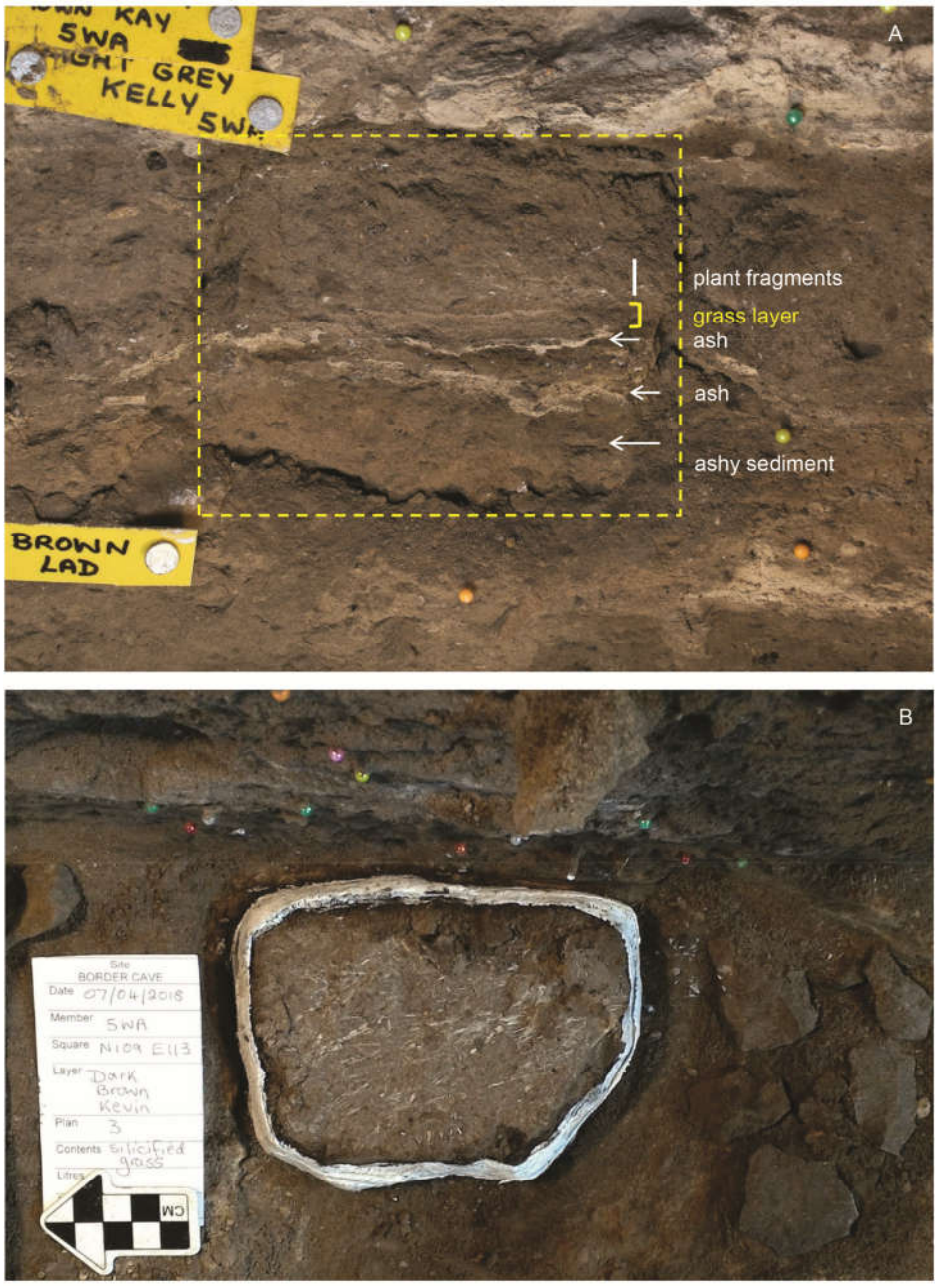

Fig. S3.

Border Cave Member 5 WA plant bedding sampled vertically and horizontally. **(A)** Vertical section in the field showing bedding on top of ash. The yellow box marks where the micromorphological block was cut from layer 5WA-DBK for the thin sections in Fig. 4 and fig. S15. The field interpretations are labelled. The layer marked 'ashy sediment' is 5WA-VPBK. **(B)** Horizontal view of silicified grass bedding 5WA-DBK removed in a plaster jacket.

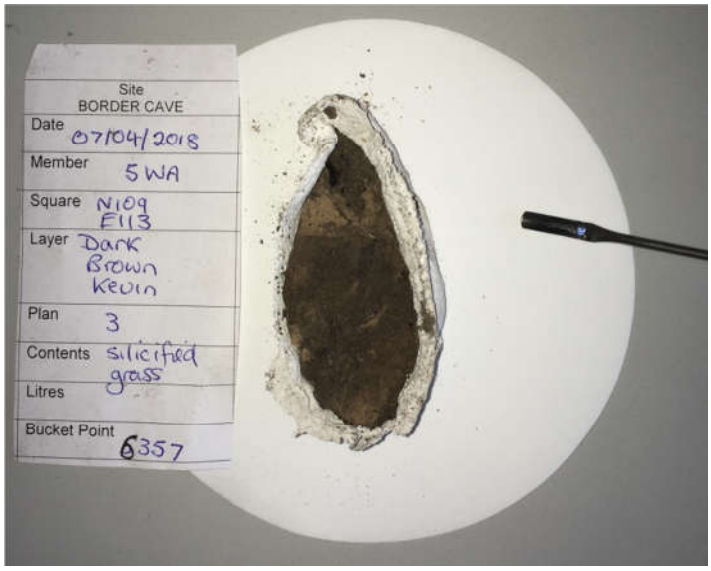

Fig. S4.
Border Cave micromorphological block for phytolith study (base view). The context is Square N109, E113, 5WA-DBK, Plan 3, BP 6357.

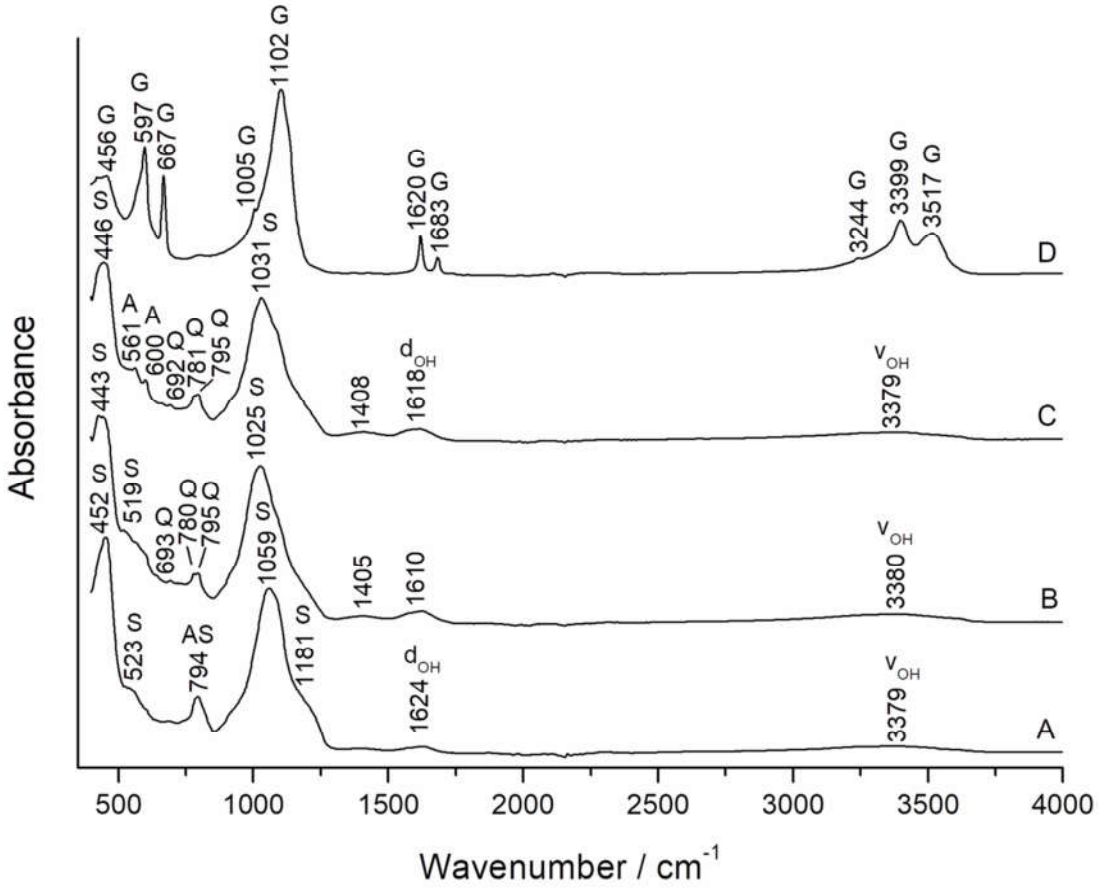

Fig. S5.

Fourier Transform Infrared (FTIR) spectra of items from layer 5WA-DBK. **(A)** Siliceous plant fibres. **(B)** Sediment sample containing plant material. **(C)** Beige sediment within the 5 WA bedding from square N109 E113. **(D)** Nodule of white gypsum powder. A = apatite, AS = amorphous silica, d_{OH} = bending vibrations of hydroxyl groups, G = gypsum, Q = quartz, S = silicates and v_{OH} = stretching vibrations of hydroxyl groups.

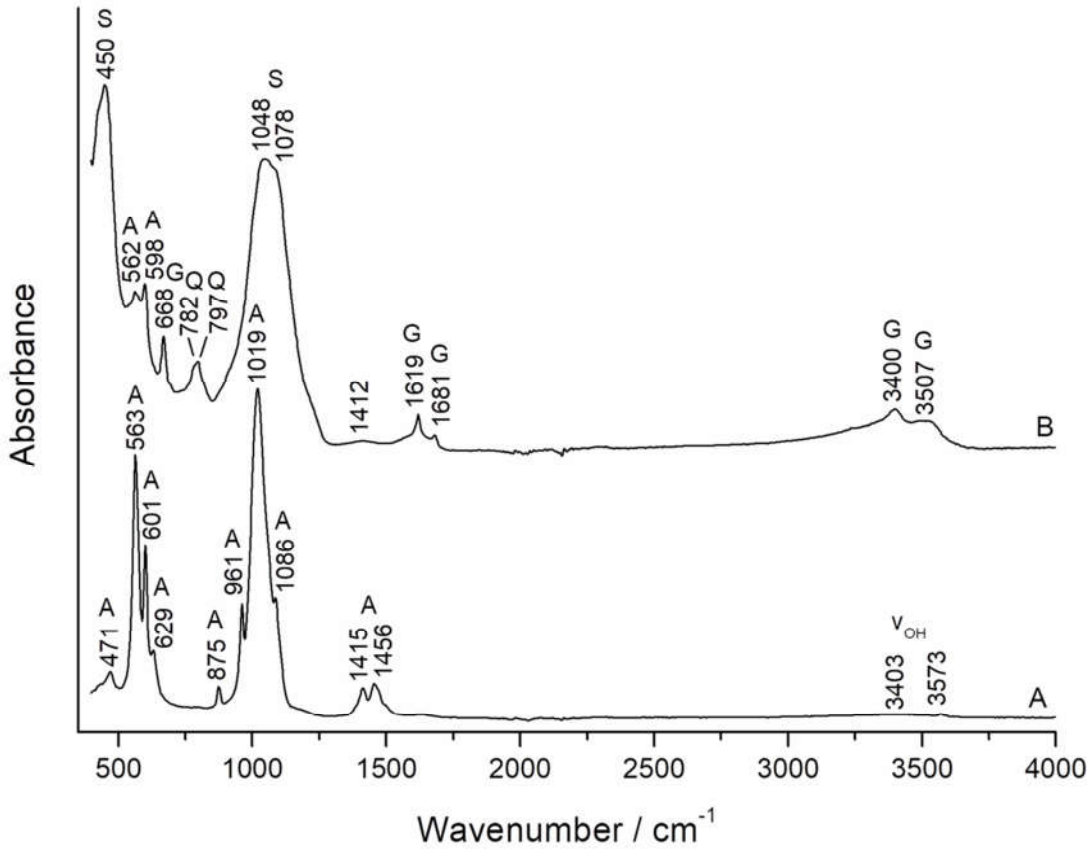

Fig. S6.

ATR-FTIR spectra of 5WA-VPBK deposits (BP6405). (A) Compacted pale yellow sediments (white pellet). **(B)** Loose sediment (sediment in bulk). A = apatite, G = gypsum, Q = quartz, S = silicates and ν_{OH} = stretching vibrations of hydroxyl groups.

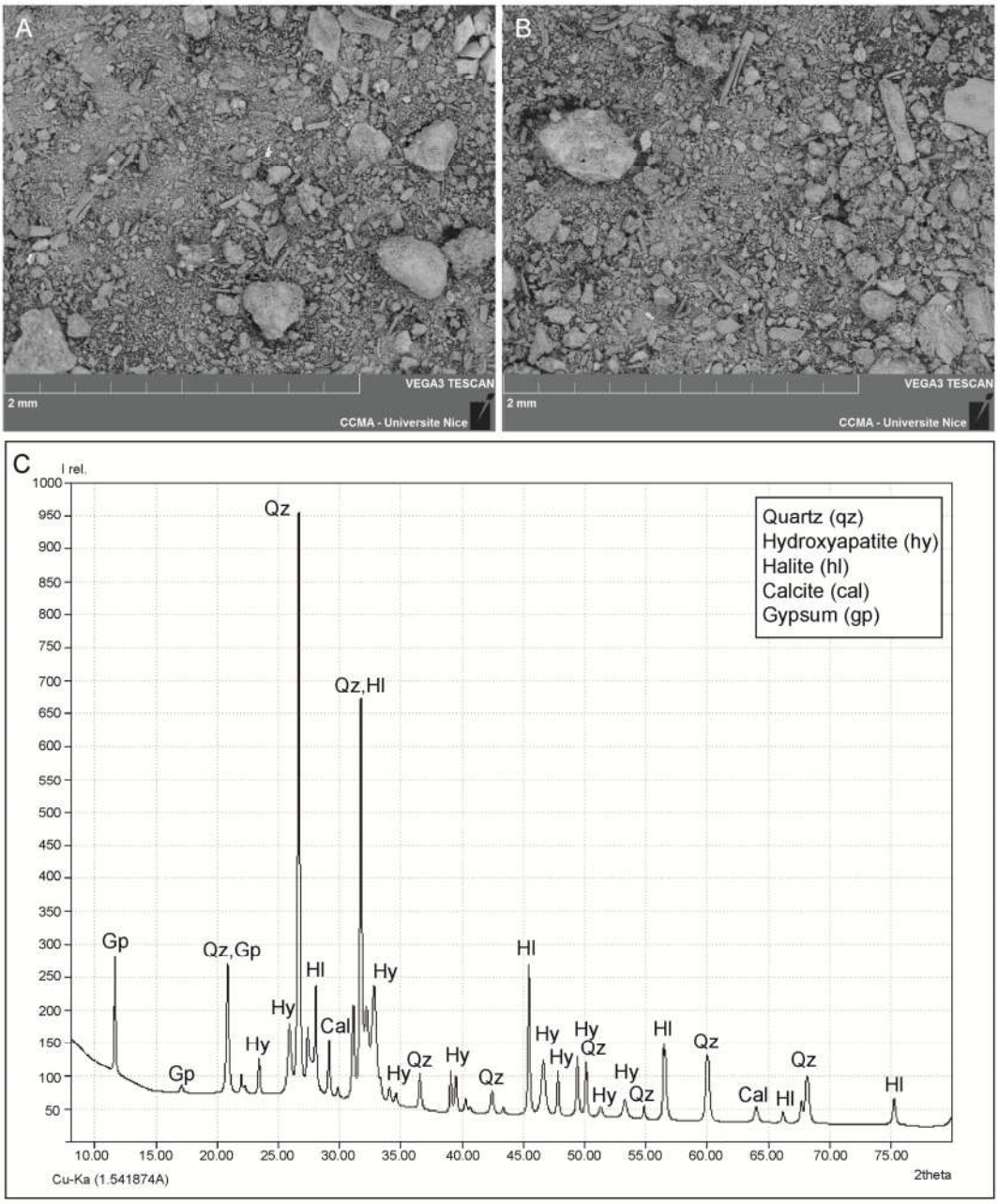

Fig. S7.
SEM images in backscattered mode (A and B) and X-ray diffractogram (C) of sediment sample from 5WA-VPBK.

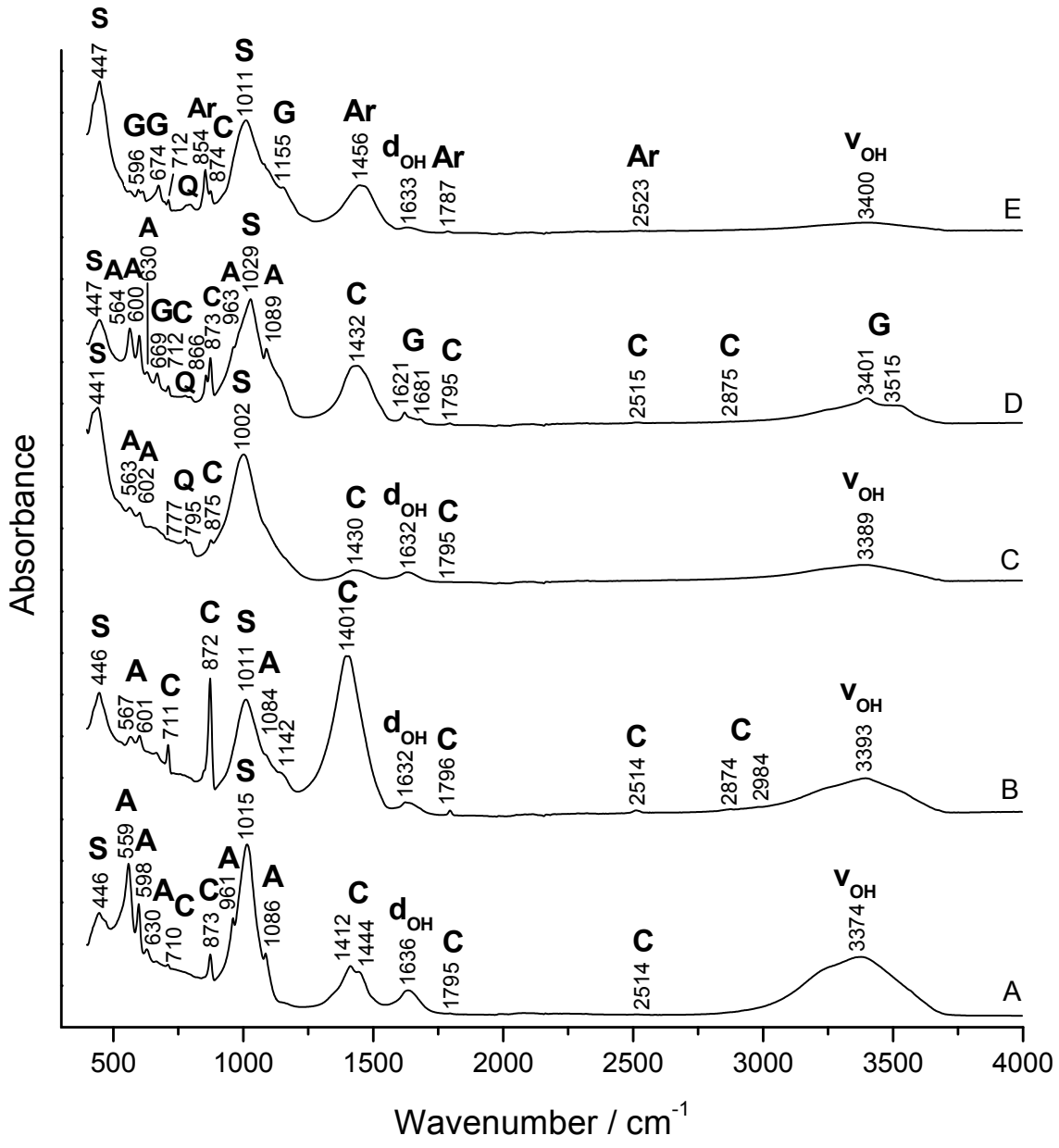

Fig. S8.

ATR-FTIR spectra of a selection of Border Cave ashy layers under plant bedding. (A) Member 1 WA, layer Barry, sample 1. **(B)** Member 2 WA, white ash top under Member 2 BSL grass bedding - see also Fig. S9. **(C)** Member 3 WA, sample 1. **(D)** Member 4 WA, layer White 3. **(E)** Member 5 BS, layer Jan, sample 2.

A = apatite, Ar = aragonite, C = calcite, d_{OH} = bending vibrations of hydroxyl groups, G = gypsum, Q = quartz, S = silicates and v_{OH} = stretching vibrations of hydroxyl groups.

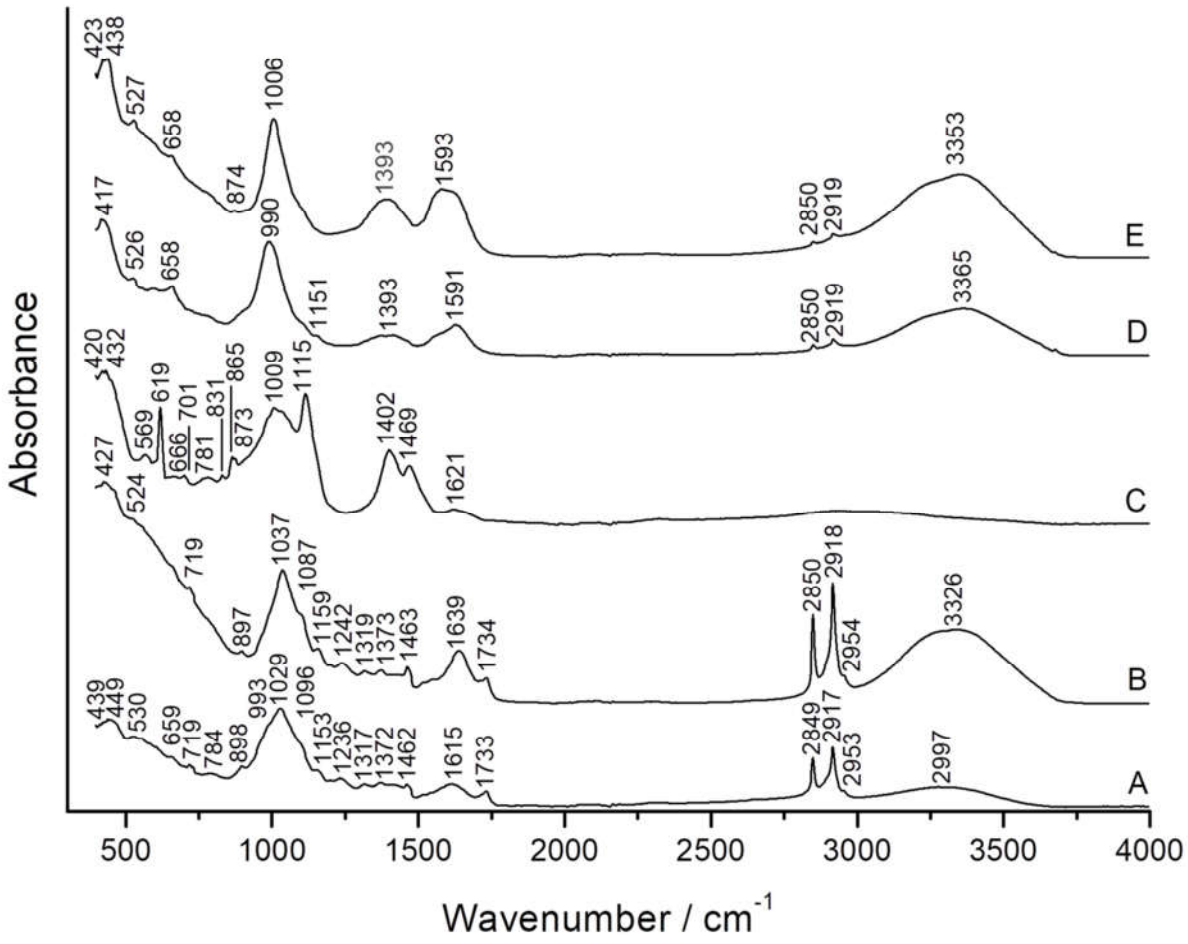

Fig. S9.

ATR-FTIR spectra of modern *Panicum maximum* and Border Cave grass bedding. (A) Modern fresh *Panicum maximum.* **(B)** Modern dried *Panicum maximum.* (**C**) Modern *Panicum maximum* ashes. **(D)** Member 2 WA, layer Dossy grass bedding. **(E)** Member 2 BSL grass bedding (see text for vibrational bands description).

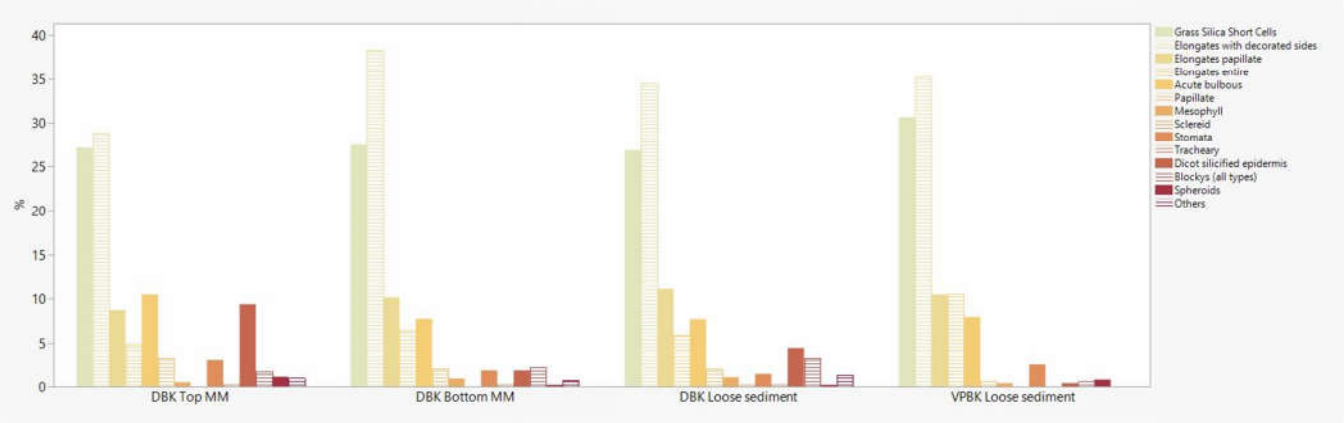

Fig. S10.

Histogram showing the phytolith morphological distribution, by plant types and plant parts, among samples from 5WA-DBK and 5WA-VPBK.

MM = micromorphological block (BP6357). 'Acute bulbous' includes trichomes and prickles. Others include indeterminates and irregular morphologies.

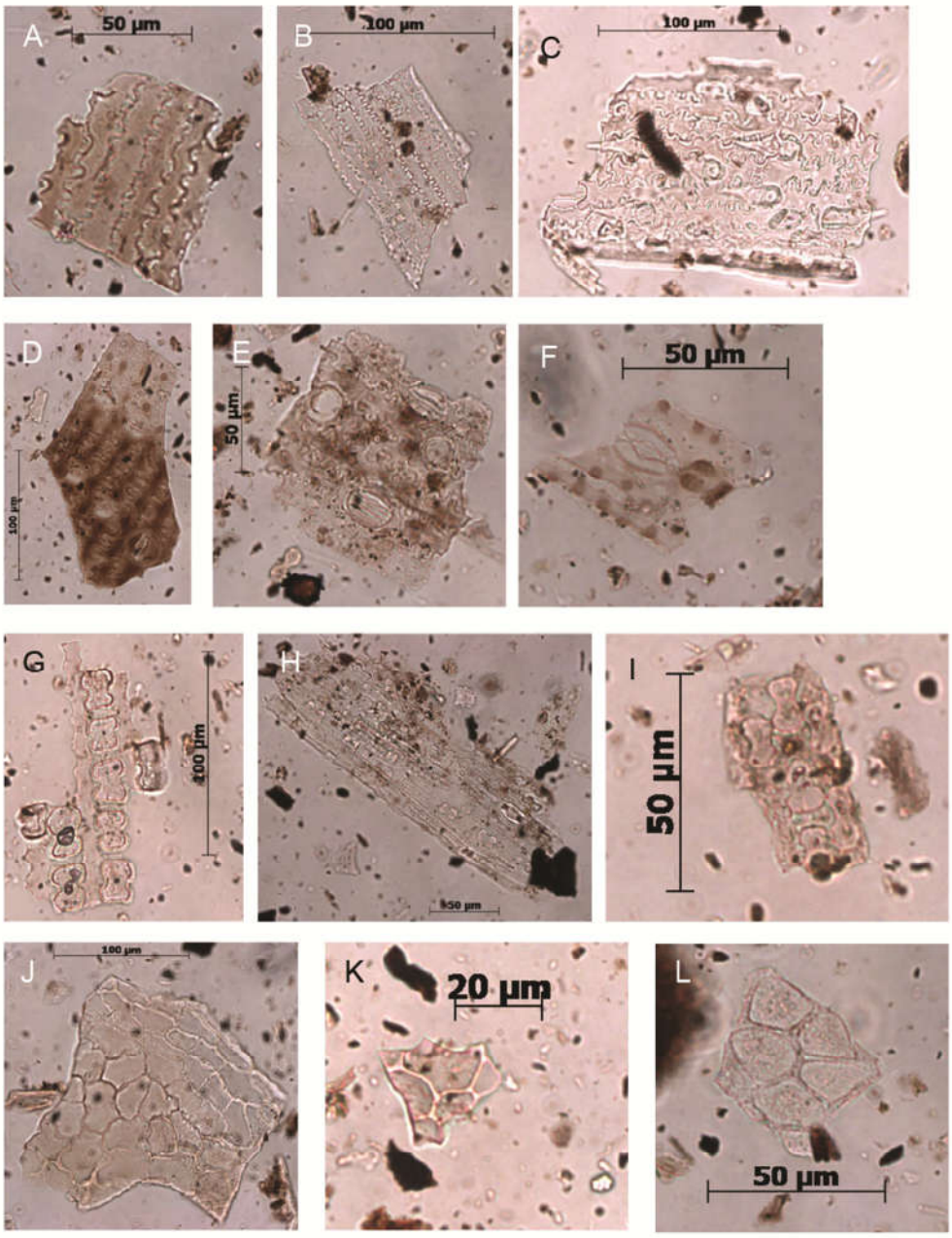

Fig. S11.
Microphotographs of phytoliths identified in micromorphology (MM) samples from 5WA-DBK. Pictures taken at 400x. (**A, B**) Interconnected cell structures of long cells with columellate/ligulate sides from sample 5WA-DBK, N109, E113, Plan3, Top MM. (**C**) Interconnected cell structures of long cells with columellate/ligulate sides together with prickles from sample 5WA-DBK, N109, E113, Plan3, Top MM. (**D-F**) Interconnected cell structures of multi-papillate long cells with columellate/ligulate sides together with stomata from sample 5WA-DBK, N109, E113, Plan3, Top MM. (**G-I**) Short cell bilobates in connection with other epidermal cells from sample 5WA-DBK, N109, E113, Plan3, Top MM. (**J**) Dicot articulated epidermal cells sinuate from sample 5WA-DBK, N109, E113, Plan3, Top MM. (**K**) Dicot articulated epidermal cells polyhedral from sample 5WA-DBK, N109, E113, Plan3, Bottom MM. (**L**) Dicot hair base and articulate epidermal cells polyhedral from sample 5WA-DBK, N109, E113, Plan3, Top MM.

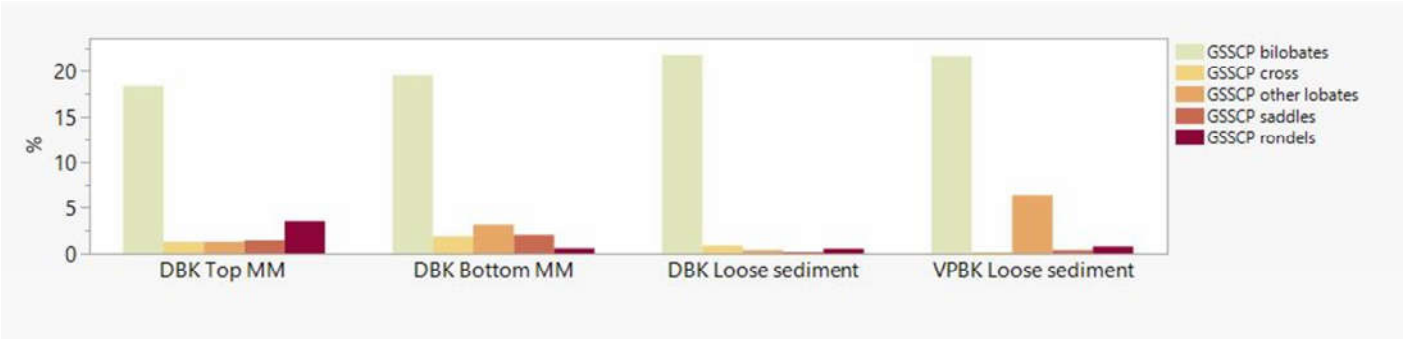

Fig. S12.

Histograms showing the grass silica short cell distribution in sediment samples from 5WA-DBK and 5WA-VPBK.

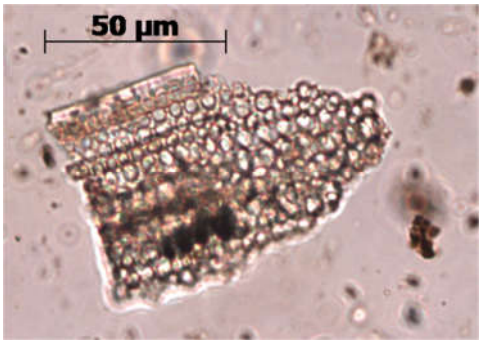

Fig. S13.
Grass leaf structures showing the upper epidermis and the palisade mesophyll in 5WA-DBK bedding.

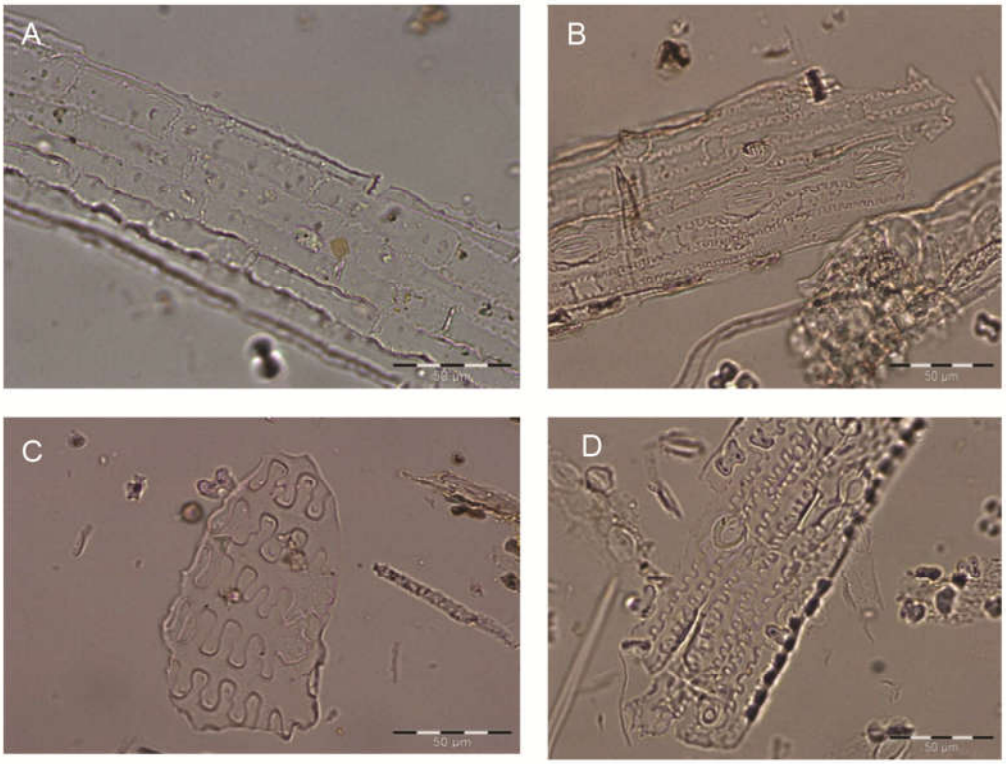

Fig. S14.

Modern grass epidermis phytoliths. (**A**) Articulated multi-papillate long cells with sinuate sides from *Themeda triandra* [elongate tuberculate in (*38*)]. (**B**) Articulated long cells with columellate/ligulate sides from *Panicum deustum* [Elongate wavy in (*38*)]. (**C**) Articulated long cells with columellate/ligulate sides from *Setaria sphacelata* [Elongate wavy in (*38*)]. (**D**) Articulated long cells with columellate/ligulate sides from *Heteropogon contortus* [Elongate wavy in (*38*)].

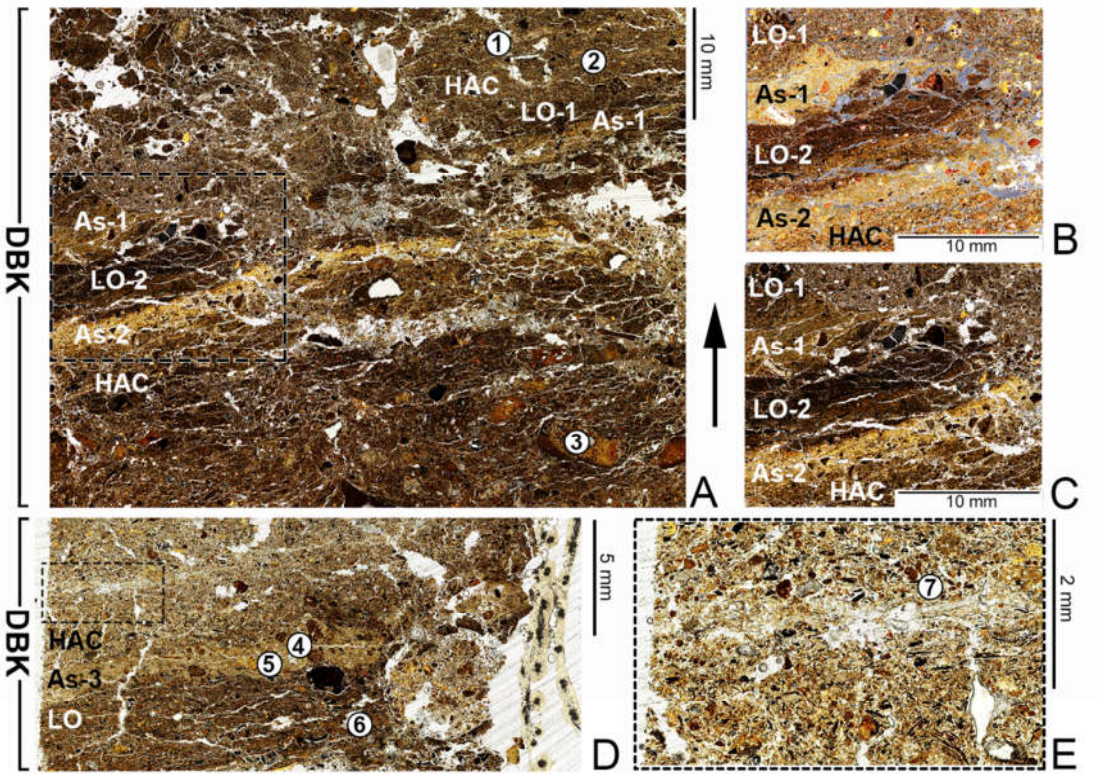

Fig. S15.
Border Cave 5WA-DBK thin sections 1/2 and 1/1 showing plant bedding traces and ash lenses.

Thin section 1/2: **(A)** Microphotograph of alternating sequence of microfacies including homogeneous anthropogenic components (HAC), ash (As-1 and As-2) and dark brown laminar units rich in organic matter (LO). **(B)** Microfacies and contacts identified in (A) by a black-dashed square, cross-polarised light (XPL) and **(C)** plane polarized light (PPL).

Thin section 1/1: **(D)** Silicified, laminar plant bedding layer within HAC, 5 mm above As-3, overlying dark brown laminar unit rich in organic matter (LO), PPL. **(E)** Magnified microphotograph of silicified, laminar bedding in black-dashed square (D), PPL.

Features 1-7: **1** and **2.** remnants of laminar plant material in HAC. **3.** Rhyolite roof spall. **4.** Rounded aggregate particles within microfacies As-3. **5.** Burnt bone fragmented in situ within As-3. **6.** Charcoal stringer in LO. **7.** Rounded, rubified particles in HAC.

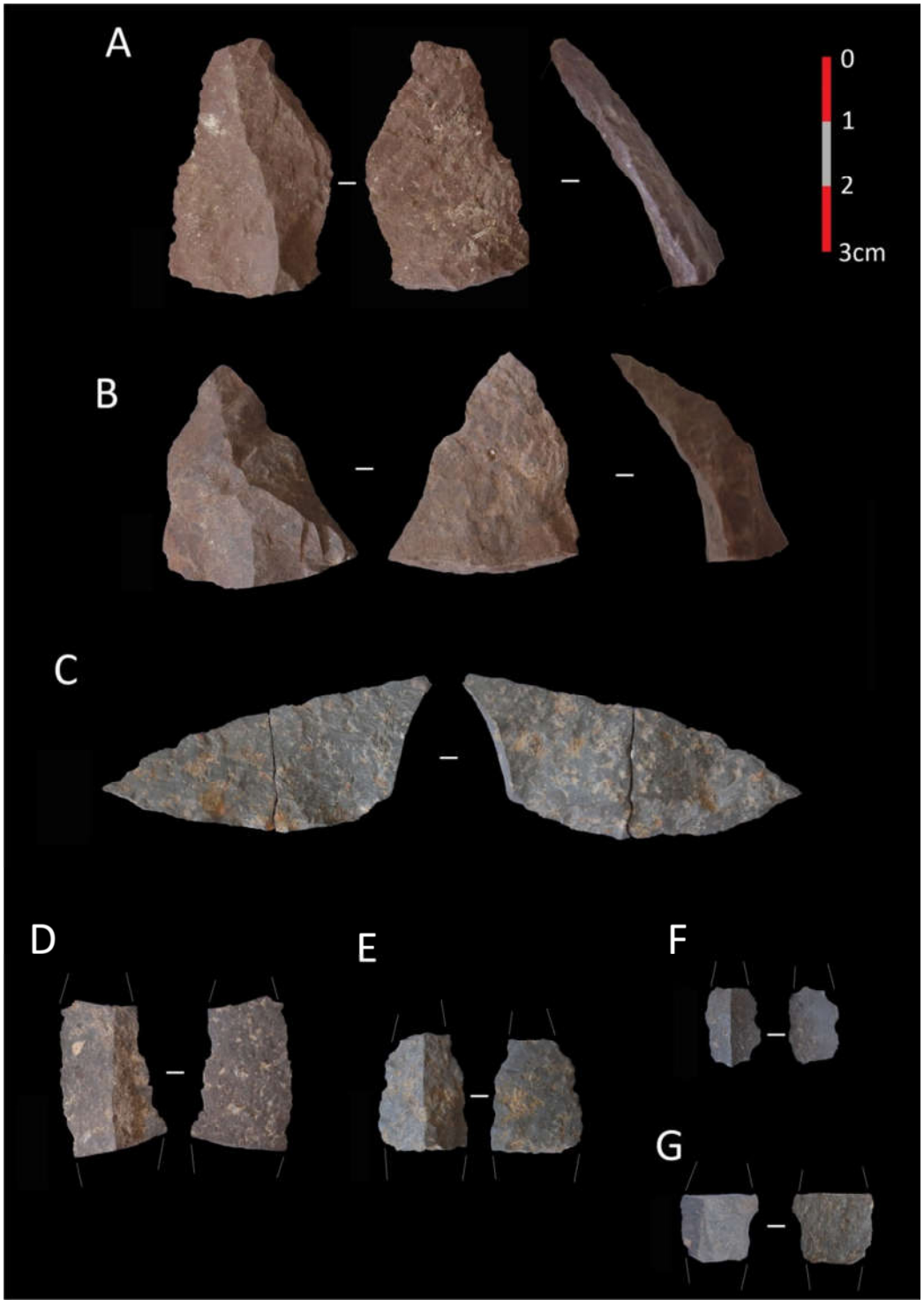

Fig. S16.

Selection of stone artefacts from 5WA-DBK. (**A** and **B**) Triangular flake blanks in hornfels. (**C**) Refitted hinge flake in rhyolite. (**D-G)** Bladelet fragments in rhyolite.

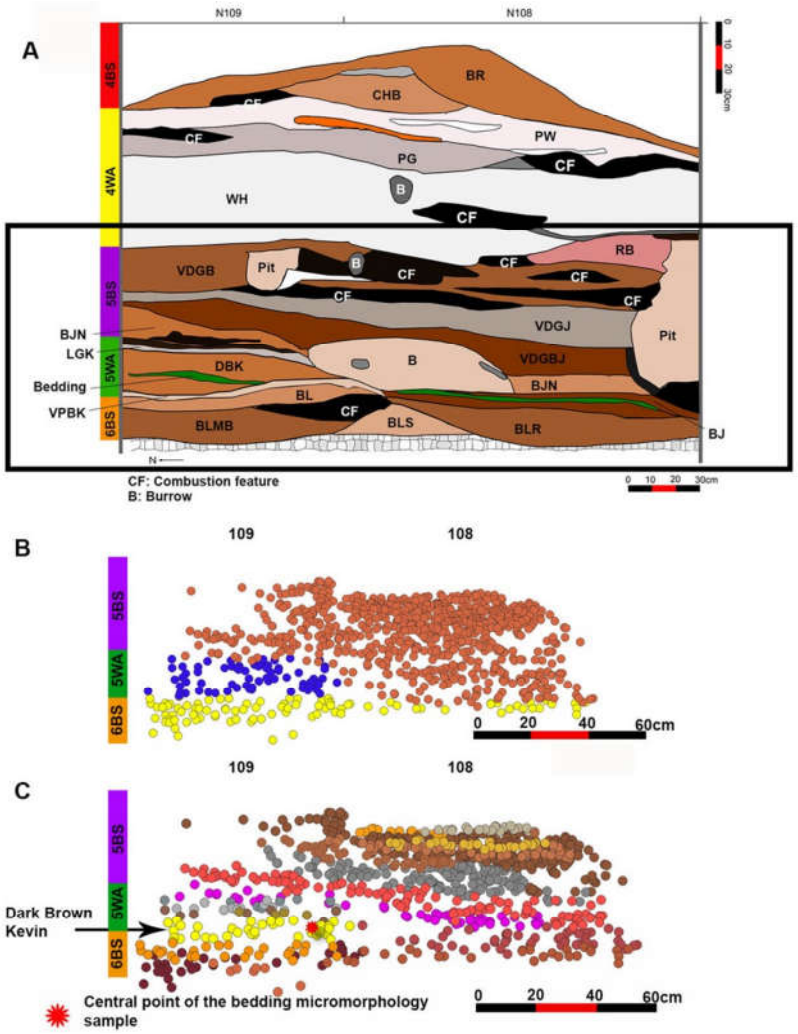

Fig. S17.

Border Cave plotting of lithics, bone and charcoal pieces >2 cm in Members 5 BS, 5 WA and 6 BS. (A) East wall profile of Squares N109 and N108 E113 showing stratigraphy in Members 4 BS to 6 BS. Scale, 30 cm. **(B)** Plotting of all items >2 cm by member (Members 5 BS, 5 WA and 6 BS). 5 **(C)** Plotting of all items >2 cm in each layer of Members 5 BS, 5 WA and 6 BS. In 5WA-DBK only lithics were present for plotting. Scale, 60 cm.

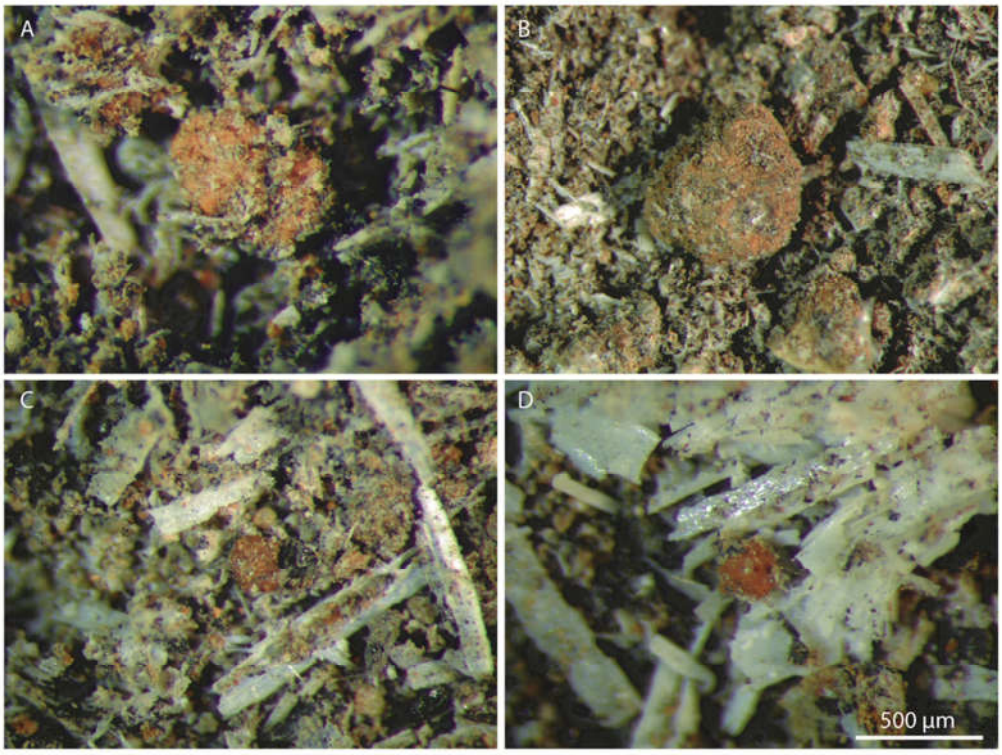

Fig. S18.
Orange and red microagglomerates from the plant bedding in layer 5WA-DBK.

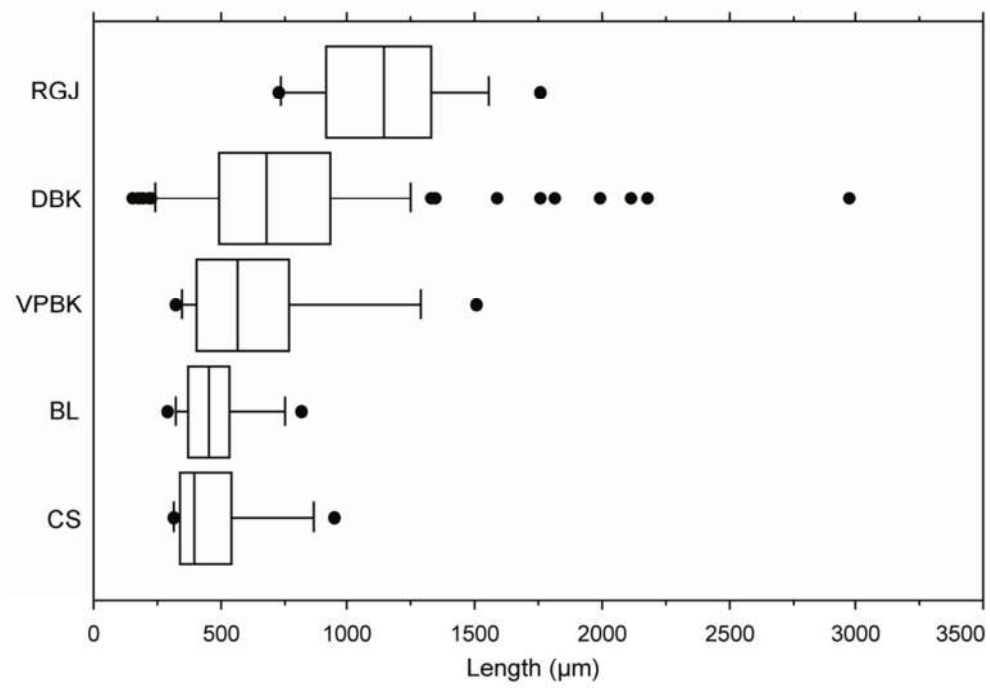

Fig. S19.

Length variation of coloured microagglomerates according to provenance (RGJ: Reddish Brown John; DBK: 5WA-DBK; VPBK: 5WA-VPBK; BL: Brown Lad; CS: control sediment).

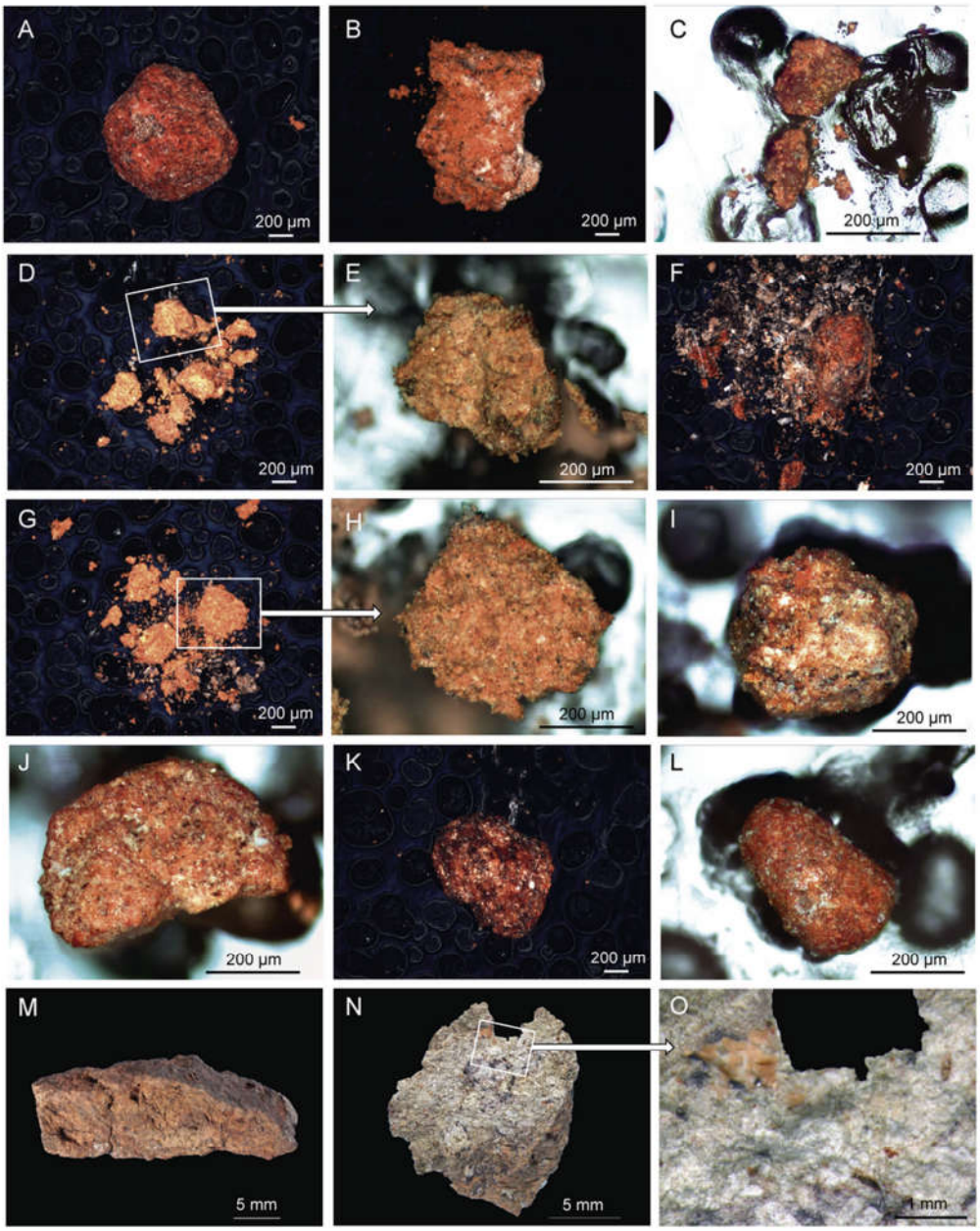

Fig. S20.

Samples analysed by SEM-EDS and µ-RS. **(A-L)** Coloured microagglomerates. (**M**) Possible ochre fragment. (**N-O**) Roof spall. Contexts: A: sample 43 (Layer Reddish Grey John); B: sample 44 (layer Reddish Grey John); C: sample 3 (layer 5WA-DBK); D-E: sample 7 (layer 5WA-DBK); F: sample 28 (layer 5WA-DBK); G-H: sample 10 (layer 5WA-DBK); I: sample 38 (layer 5WA-VPBK); J: sample 42 (layer Brown Lad); K: sample 39 (control sediment); L: sample 40 (control sediment); M: sample OF1 (layer 5WA-DBK); N: sample RS1 (roof spall from control sediment).

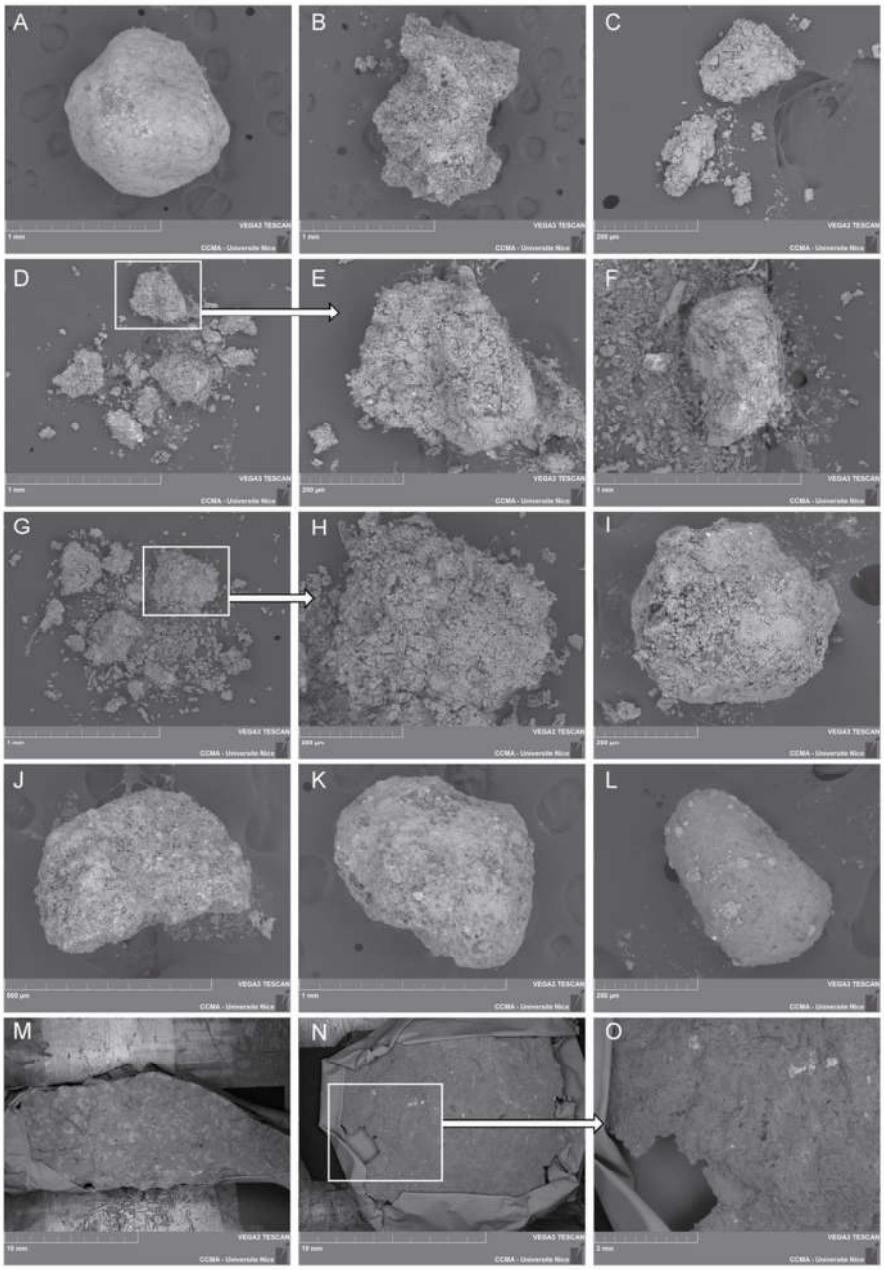

Fig. S21.

SEM images of coloured microagglomerates (A-L), a possible ochre fragment (M) and a roof spall (N-O). All figures are in backscattered mode. Contexts: A: sample 43 (Layer Reddish Grey John); B: sample 44 (layer Reddish Grey John); C: sample 3 (layer 5WA-DBK); D-E: sample 7 (layer 5WA-DBK); F: sample 28 (layer 5WA-DBK); G-F: sample 10 (layer 5WA-DBK); I: sample 38 (layer 5WA-VPBK); J: sample 42 (layer Brown Lad); K: sample 39 (control sediment); L: sample 40 (control sediment); M: sample OF1 (layer 5WA-DBK); N: sample RS1 (roof spall from control sediment).

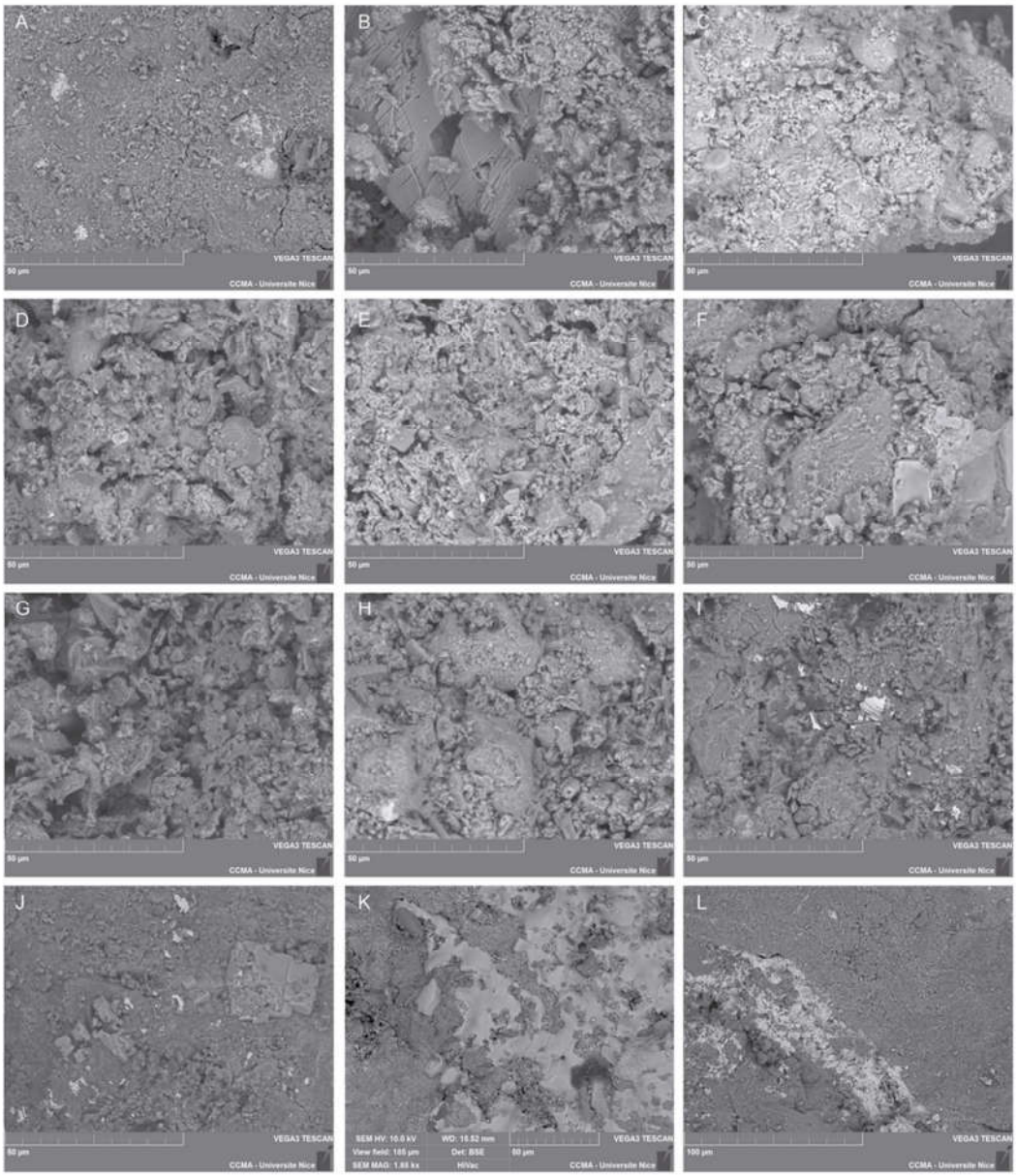

Fig. S22.

SEM images of coloured microagglomerates (A-J), a possible ochre fragment (K), and a roof spall (L). All figures are in backscattered mode. Contexts: A: sample 43 (Layer Reddish Grey John); B: sample 44 (layer Reddish Grey John); C: sample 3 (layer 5WA-DBK); D: sample 7 (layer 5WA-DBK); E: sample 10 (layer 5WA-DBK); F: sample 28 (layer 5WA-DBK); G: sample 38 (layer 5WA-VPBK); H: sample 42 (layer Brown Lad); I: sample 39 (control sediment); J: sample 40 (control sediment); K: sample OF1 (layer 5WA-DBK); L: sample RS1 (roof spall from control sediment).

Table S1.

Beaumont's naming system of the Border Cave members together with a summary of the ^{14}C and Electron Spin Resonance (ESR) dates. For calibrations and methods, see (*17, 18, 83-86*).

Member	Layer	Industry	Age (ky ago)	Dating method	Ref.
1 BS	UP	ELSA	-	-	-
	Lower A		41.5 - 24	^{14}C	(*83*)
	Lower B		42.3	^{14}C	(*83-85*)
	Lower C		42.6	^{14}C	(*83-85*)
1 WA	UP	ELSA	43	^{14}C	(*83, 85*)
	2		-	-	-
2 BS	UP	MSA 3	49.0 - 44.2	^{14}C	(*85*)
	Lower A-C		49.0 - 60.0 *	^{14}C	(*85*)
2 WA		MSA 3	60 ± 3 *	ESR	(*17, 85*)
3 BS	1	HP	56 ± 2	ESR	(*17, 86*)
	2		64 ± 3	ESR	(*17, 86*)
	3		72 ± 4	ESR	(*17, 86*)
3 WA		HP	64 ± 2	ESR	(*17, 86*)
1 RGBS		HP	74 ± 4	ESR	(*17, 86*)
4 BS		MSA 1	77 ± 2	ESR	(*17, 86*)
4 WA	1	MSA 1	115 ± 8	ESR	(*17, 86*)
	6		113 ± 5	ESR	(*17, 86*)
	7		168 ± 5	ESR	(*17, 86*)
5 BS	2	MSA 1	161 ± 10	ESR	(*17, 86*)
	5		144 ± 11	ESR	(*17, 86*)
5 WA	1	MSA 1	183 ± 20	ESR	(*17, 86*)
	2		227 ± 11	ESR	(*17, 86*)
6 BS	1	MSA 1	-	-	-

* the ^{14}C ages for Members 2 WA, 2 BS Lower C and B, ranging from 58 to 48 ky ^{14}C BP, fall outside of the range of the IntCal09 calibration curve.

Table S2.

Border Cave plant bedding features in each member. Some desiccated bedding has burned patches within it. A grass bedding sample from Member 1 BS Lower C (#242), Grass Bed 2A, was radiocarbon dated to 36,700 ± 900 B.P. [37,640 cal B.C.] (OxA-33715). A grass bedding sample from Member 2 BS UP (#796), Grass Bed 1, was radiocarbon dated to 43,300 ± 2700 B.P. (OxA-33716) (*13*).

Member	Layer/Feature	Colour	Desiccated/Burned
1BS.LR.C	Grass Bed 1	5YR3/2	Desiccated & Burned
	Grass Bed 2	7YR4/2	Desiccated & Burned
	Grass Bed 3	-	Desiccated
	Dark Reddish Brown Ally Grass Bed	5YR2.5/2	Desiccated
1WA	Grass Bed 2, Caramel Bed 1	-	Desiccated
	Betty Grass Bed	-	Desiccated
	White Bifi Grass Bed	5YR8/1	Desiccated
	Bill Grass Bed	-	Desiccated
	Bimba Grass Bed	-	Desiccated & Burned
	Bingo Grass Bed	-	Desiccated
	Bob Grass Bed	-	Desiccated
	Dark Brown Bobby Grass Bed	7.5YR3/3	Desiccated
	Dark Brown Botha Grass Bed	7.5YR3/3	Desiccated
	Grey Bride Grass Bed	7YR5/1	Desiccated
2BS.UP	Grass Bed 1	-	Desiccated & Burned
	Grass Bed 2 and Combustion Feature 1	-	Desiccated & Burned
	Camilla Grass Bed	10YR5/4	Desiccated
	Camilla 2 Grass Bed	10YR5/4	Desiccated
	Carly Grass Bed	-	Desiccated
	Carrol Grass Bed	-	Desiccated
	Cassidy Grass Bed	10YR4/3	Desiccated
2BS.LR.A	Ceta Grass Bed	10YR4/4	Desiccated
2BS.LR.C	Grass Bed 1	-	Desiccated & Burned
	Grass Bed 2	-	Desiccated
	Grass Bed 3	-	Desiccated
	Cilla Grass Bed	-	Desiccated & Burned
2WA	Brown Dan Grass Bed	10YR5/3	Desiccated
	Davos Grass Bed	7.5YR4/3	Desiccated
	Decon Grass Bed	-	Desiccated
	Delta Grass Bed	7.5YR4/3	Desiccated
	Denia Grass Bed	7.5YR4/4	Desiccated
	Reddish Black Desmond 1,2 Grass Bed	2.5YR2.5/1	Desiccated
	Dark Brown Devan Grass Bed	-	Desiccated
	Brown Dia Grass Bed	7.5YR4/3	Desiccated
	Dark Brown Dijon	-	Burned
	Brown Don Grass Bed	-	Desiccated
	Dark Yellowish Brown Dossy Grass Bed	10YR3/6	Desiccated
	Dossy Grass Bed	-	Desiccated
	Greyish-brown Duran Grass Bed	-	Desiccated & Burned
3BS.LR.B	Eaton Grass Bed	5YR3/3/3	Burned
	Dark Grey Ebo2 Grass Bed	-	Burned
	Eco Grass Bed	-	Burned
	Ega Grass Bed	-	Burned
3WA	Black Fade Grass Bed	5YR2.5/1	Desiccated
1RGBS	Very Dark Brown Faan Grass Bed	-	Desiccated & Burned
5BS	Brown Jolly Grass Bed	7.5YR4/2	Silicified & Burned
5WA	DBK (Dark Brown Kevin) Grass Bed	5YR3/2	Silicified & Burned

Table S3.
Major (wt %) and trace element (µg/g) data obtained by energy dispersive X-ray fluorescence analyses on sediment sample from layer 5WA-VPBK.

Si (%)	27,91
K (%)	1,315
Ca (%)	3,695
Ti (%)	0,1747
V (µg/g)	< 2,1
Cr (µg/g)	< 2,4
Mn (%)	0,08611
Fe (%)	1,752
Ni (µg/g)	17,6
Zn (µg/g)	74,3
Ga (µg/g)	10,6
As (µg/g)	8,1
Rb (µg/g)	60,8
Sr (µg/g)	275,7
Y (µg/g)	48,1
Zr (µg/g)	869,7
Ba (µg/g)	555,4
Pb (µg/g)	< 2,0
Th (µg/g)	10,6
U (µg/g)	< 0,6

Table S4.
Results of SEM-EDS analyses on sediment sample from layer 5WA-VPBK.

Sam	Num of an	Description of analysed item				Semi-quantitative EDX analyses **				Interpretation
		Grain morph	BSE cont*	Length range (µm)	Width range (µm)	>10%	10-3%	3-1%	<1%	
VPBK sed	3	Elon / Irr	LG / G	142-183	30-110	Si, C	-	(Ca, P, Cl)	(Al, Na, K, Mg, Fe, S)	grass material
VPBK sed	2	Irr	LG / G	67-168	40-110	C, Ca (S)	(Si)	-	(Al, P, Na, Cl, Fe, K, Mg)	calcium carbonate
VPBK sed	3	Irr / ang	LG	67-536	12-400	Ca (C)	P (Si)	(Cl, Na, Al)	(K, Mg, S, Fe)	calcium phosphate
VPBK sed	1	Irregular	W	67	21	Ba (C, Si)	S	(Al, K, Ca)	(Na, P, Mg, Cl, Ti)	barium sulphate
VPBK sed	2	Irr	W/LG	23-47	20-26	Cl (C) Na	(Si)	(Ca)	(P, Al, Fe, K, Mg, Ti)	sodium chloride
VPBK sed	4	Irr / ang	LG / G	64-144	40-105	Si (C)	(Al)	(Ca, Fe, K, P, Na)	(Cl, Mg, S, Ti)	silicate
VPBK sed	4	Aggl	G	-	-	C, Si	Ca	P, Al, Cl, Fe	Na, K, Mg, S, Ti, Mn	silicates + calcium carbonates

Sam: sample; VPBK sed: Very Pale Brown Kim sediment; num: number; an: analyses; morph: morphology; cont: contrast; elon: elongated; irreg: irregular; ang: angular; aggl: agglomerate; LG: light grey; G: grey; W: white.

(*): BSE cont. refers to the contrast observed on backscattered electron (BSE) images.

Table S5.

Phytolith concentration in square N109, E113, layer 5WA-DBK and 5WA-VPBK. Phytolith concentration per gram of sediment, the total number of phytoliths counted per sample and the percentage of articulated phytoliths, as well as the average, maximum and minimum of cells per articulated phytoliths. **MM =** micromorphological block; **BP** = bucket point; sed. = sediment.

	5WA-DBK Plan 3			**5WA-VPBK**
Sample	**Top MM (BP 6357)**	**Bottom MM (BP 6357)**	**Loose sediment**	**Loose sediment**
Phytoliths counted per sample	626	540	554	516
Phytoliths per gram sed. in million	92,1	107,3	55,4	70,5
% Articulated phytoliths	62,3	57,2	62,1	64,3
Average number of cells per articulated phytoliths	6,1	4,6	5,2	5,2
Maximum number of cells per articulated phytoliths	46	17	54	16
Minimum number of cells per articulated phytoliths	2	2	2	2

Table S6.

Phytolith morphology.

List of phytolith morphotypes identified, ICPN 2.0 nomenclature (*43*), their taxonomic affiliation and their frequencies in samples from square N109, E113, layer 5WA-DBK and 5WA-VPBK. MM = micromorphological block (BP6357).

Morphotypes	**ICPN 2.0**	**Taxonomic affiliation**	**5WA-DBK Plan 3**			**5WA-VPBK**
			Top MM	**Bottom MM**	**Loose sediment**	**Loose sediment**
Articulated phytolith indeterminate		Dicot leaves	0,00	0,00	2,68	0,19
Articulated phytolith jigsaw	AREOLATE/FAVOSE	Dicot leaves	0,63	0,00	0,00	0,00
Articulated phytolith polyhedral	POLYGONAL	Dicot leaves	1,11	1,10	1,61	0,00
Articulated phytolith polyhedral elongate	POLYGONAL ELONGATE	Dicot leaves	0,00	0,74	0,00	0,00
Articulated phytolith sinuate	SINUATE	Dicot leaves	7,29	0,00	0,00	0,00
Blocky *sensu lato*		Non-diagnostic	0,00	0,18	0,00	0,00
Blocky polyhedral		Non-diagnostic	0,95	1,10	1,25	0,19
Blocky polyhedral echinate/papillate		Non-diagnostic	0,16	0,37	0,00	0,00
Cane - epidermal appendage or sclereid		Unidentified	0,63	0,55	0,89	0,00
Elongate	ELONGATE ENTIRE	Non-diagnostic	4,12	5,71	5,01	10,47
Elongate aculeate/ligulate	ELONGATE ACULEATE/LIGULATE	Poaceae	1,27	3,87	1,61	13,95
Elongate aculeate/ligulate papillate	ELONGATE ACULEATE/LIGULATE PAPILLATE	Poaceae	0,00	0,55	0,00	0,00
Elongate blocky	ELONGATE BLOCKY/THICK	Non-diagnostic	0,32	0,00	1,25	0,19
Elongate blocky echinate	ELONGATE BLOCKY ECHINATE	Poeaceae?	0,00	0,00	0,00	0,19
Elongate blocky facetate	ELONGATE BLOCKY FACETATE	Non-diagnostic	0,32	0,18	0,36	0,00
Elongate blocky facetate echinate	ELONGATE BLOCKY FACETATE ECHINATE	Non-diagnostic	0,00	0,18	0,00	0,00
Elongate castellate	ELONGATE CASTELLATE	Poaceae	1,11	0,00	0,00	0,00
Elongate clavate	ELONGATE CLAVATE	Poaceae	1,27	0,18	2,50	6,59
Elongate clavate papillate	ELONGATE CLAVATE PAPILLATE	Poaceae	0,63	1,66	0,00	0,97
Elongate columellate/ligulate	ELONGATE COLUMELLATE/LIGULATE	Poaceae	9,35	14,36	11,45	2,33
Elongate columellate/ligulate	ELONGATE COLUMELLATE/LIGULA	Poaceae	2,69	6,08	6,26	0,00

papillate	TE PAPILLATE					
Elongate columellate/ligulate striate	ELONGATE COLUMELLATE/LIGULATE STRIATE	Poaceae	1,74	0,00	0,00	0,00
Elongate crenate	ELONGATE CRENATE	Poaceae	1,43	4,24	0,00	6,59
Elongate crenate papillate	ELONGATE CRENATE PAPILLATE	Poaceae	0,00	1,84	0,00	0,00
Elongate curved	ELONGATE CURVED	Poaceae	0,00	0,00	0,18	0,00
Elongate dendritic	ELONGATE DENDRITIC	Poaceae	0,79	0,00	0,00	0,00
Elongate dendritic papillate	ELONGATE DENDRITIC PAPILLATE	Poaceae	1,11	0,00	0,00	0,00
Elongate dentate	ELONGATE DENTATE	Poaceae	0,00	1,84	0,00	0,00
Elongate dentate papillate	ELONGATE DENTATE PAPILLATE	Poaceae	0,00	0,00	0,18	0,00
Elongate echinate/aculeate	ELONGATE ECHINATE/ACULEATE	Poaceae	1,90	0,74	3,58	1,16
Elongate echinate/aculeate papillate	ELONGATE ECHINATE/ACULEATE PAPILLATE	Poaceae	0,00	0,00	0,00	1,36
Elongate facetate	ELONGATE FACETATE	Poaceae	0,48	0,37	0,72	0,00
Elongate lacunose	ELONGATE LACUNOSE	Poaceae	0,16	0,18	0,00	0,00
Elongate laminate	ELONGATE LAMINATE	Poaceae	0,16	0,18	0,00	0,00
Elongate ligulate	ELONGATE LIGULATE	Poaceae	1,27	0,00	5,55	0,58
Elongate ligulate papillate	ELONGATE LIGULATE PAPILLATE	Poaceae	0,00	0,00	0,00	2,33
Elongate pilate	ELONGATE PILATE	Poaceae	0,16	0,18	0,00	0,00
Elongate polylobate	ELONGATE POLYLOBATE	Poaceae	0,00	0,00	0,18	0,00
Elongate sinuate	ELONGATE SINUATE	Poaceae	8,56	12,89	7,51	4,07
Elongate sinuate laminate	ELONGATE SINUATE LAMINATE	Poaceae	0,00	0,00	2,15	0,00
Elongate sinuate papillate	ELONGATE SINUATE PAPILLATE	Poaceae	4,28	0,00	4,65	5,81
GSSC bilobate *sensu lato*	BILOBATE	Poaceae, C_4 Panicoideae	6,97	9,58	16,99	11,43
GSSC bilobate notched lobes	BILOBATE	Poaceae, C_4 Panicoideae	3,01	2,21	1,07	1,36
GSSC bilobate flattened lobes	BILOBATE	Poaceae, C_4 Panicoideae	4,60	3,50	1,61	4,07
GSSC bilobate rounded lobes	BILOBATE	Poaceae, C_4 Panicoideae	3,80	4,24	2,15	4,84
GSSC bilobate scooped	BILOBATE	Poaceae, C_4 Chloridoideae ?	0,00	0,00	0,00	0,97
GSSC asymmetrical ends		Poaceae, C_4 Panicoideae	0,00	0,92	0,00	5,23
GSSC cross	CROSS	Poaceae, C_4 Panicoideae	1,27	1,84	0,89	0,19
GSSC oblong trapeziform sinuate	CRENATE	Poaceae, C_3 Pooideae	0,16	0,00	0,00	0,00
GSSC rondel	RONDEL	Poaceae, C_3	2,38	0,18	0,54	0,58
GSSC rondel tall	RONDEL	Poaceae, C_3	0,63	0,18	0,00	0,00
GSSC rondel wavy top	RONDEL	Poaceae, C_3	0,32	0,18	0,00	0,19
GSSC *sensu lato*	GSSCP	Poaceae	1,27	0,37	3,04	0,00

GSSC saddle	SADDLE	Poaceae, C_4 Chloridoideae	1,43	2,03	0,18	0,58
GSSC Stipa-type	BILOBATE	Poaceae, C_3	0,95	1,66	0,36	1,16
GSSC trilobate	GSSCP	Poaceae, C_4 Panicoideae	0,32	0,55	0,00	0,00
Hair base (grass)	ACUTE BULBOUS	Poaceae	0,32	0,00	0,00	0,00
Hair base (dicot)	ACUTE BULBOUS	Dicot leaves	0,16	0,00	0,00	0,00
Hair cell (prickles)	ACUTE BULBOUS	Non-diagnostic	2,22	3,50	3,04	3,49
Hair cell (trichomes)	ACUTE BULBOUS	Non-diagnostic	7,13	3,68	3,76	4,07
Hair cell (other types)	ACUTE BULBOUS	Non-diagnostic	0,63	0,55	0,89	0,39
Irregular protuberances		Dicot fruit?	0,16	0,00	0,18	0,00
Mesophyll		Non-diagnostic	0,48	0,92	1,07	0,39
Papilla	PAPILLATE	Associated to Poaceae	3,01	2,03	1,79	0,39
Papilla squared	PAPILLATE	Associated to Poaceae	0,16	0,00	0,00	0,00
Papilla large	PAPILLATE	Associated to Poaceae	0,00	0,00	0,18	0,19
Parallelepiped blocky	BLOCKY	Dicot wood/bark	0,00	0,18	0,36	0,00
Platelet		Dicot leaves	0,32	0,00	0,18	0,19
Sclereids	SCLEREID	Dicot leaves	0,00	0,00	0,18	0,00
Spheroid (cluster) dissolution?	SPHEROID	Non-diagnostic	0,95	0,00	0,00	0,00
Spheroid large	SPHEROID	Non-diagnostic	0,16	0,00	0,00	0,00
Spheroid psilate	SPHEROID	Non-diagnostic	0,00	0,18	0,18	0,19
Spheroid rugulate/verrucate	SPHEROID	Non-diagnostic	0,00	0,00	0,00	0,58
Stomata	STOMATA	Non-diagnostic	2,85	1,29	1,07	2,52
Substomatal cavity	STOMATA	Poaceae?	0,16	0,55	0,36	0,00
Tracheid	TRACHEARY ANNULATE	Dicot leaves	0,16	0,18	0,18	0,00
Vascular bundle		Non-diagnostic	0,16	0,18	0,18	0,00

Table S7.

A selection of archaeological phytolith studies that used a quantitative approach. Included is information on the region, archaeological site, the period and sample type and the highest phytolith concentration. Sed. = sediment. AIF = acid insoluble fraction. MSA = Middle Stone Age. MP = Middle Palaeolithic. UP = Upper Palaeolithic.

Region	**Site**	**Sample type and period**	**Phytolith /g of sed. or AIF (in million)**	**References**
South Africa (Western Cape)	Pinnacle Point 13B	Dark sediments (burnt), MSA	0.14	(*87*)
South Africa (Western Cape)	Pinnacle Point 5-6	Ash layer, MSA	3.7	(*88*)
South Africa (Limpopo)	Mwulu's Cave	General Archaeological layer, MSA	4.2	(*89*)
Spain (Valencia)	Abrigo de la Quebrada	Non-hearth related sediment, MP	4	(*90*)
Spain (Cantabria)	Esquilleu	Dark grey sediment and hearth, MP	2.9	(*12*)
Greece (Thessaly)	Theopetra	Hearth, MP	43	(*80*)
Spain (Valencia)	Cova de les Cendres	Greyish layer, UP	5.5	(*91*)
Spain (Álava)	Los Husos II	Fumier, Neolithic	34	(*92*)
Syria (Upper Khabur)	Tell Seker al-Aheimar	Plastered floor, Neolithic	3.9	(*93*)
Israel	Tel Dor	Room related to a large residential building, Iron Age	46	(*79*)
Israel	Tell es-Safi/Gat	Soil sediments, Iron Age	20	(*94*)
Belgium (Brussels)	Brussels	Urban Dark Earth deposits, Middle Ages	1.9	(*95*)

Table S8.
Charcoal identifications from 5WA-DBK. BP = bucket point reading from the total station.

Genus and species	Family	Charcoal specimen number
5WA-DBK, Plan 1, BP 6228		
Diospyros sp.	Ebenaceae	6228.1, 6228.2
Canthium sp.	Rubiaceae	6228.4
Tarchonanthus trilobus	Asteraceae	6228.5, 6228.6, 6228.7
unidentified	Asteraceae	6228.3
5WA-DBK, Plan 2, BP 6310		
Allophylus cf. *dregeanus*	Sapindaceae	6310.3, 6310.9, 6310.10
Cryptocarya liebertiana	Lauraceae	6310.12
Pappea capensis	Sapindaceae	6310.1, 6310.2, 6310.4, 6310.5
Tarchonanthus trilobus	Asteraceae	6310.6
unidentified	Rubiaceae	6310.7, 6310.8
unidentified	Fabaceae Caesalpiniaceae	6310.11
5WA-DBK, Plan 3, BP 6384		
Canthium cf. *inerme*	Rubiaceae	6384.4
Canthium sp.	Rubiaceae	6384.1, 6384.3, 6384.6
Mystroxylon aethiopicum	Celastraceae	6384.10
Searsia cf. *chirindensis*	Anacardiaceae	6384.5
Vangueria cf. *infausta*	Rubiaceae	6384.2
unidentified	Rubiaceae	6384.7, 6384.8, 6384.9
5WA-DBK, Plan 3, BP 6419		
Allophylus cf. *dregeanus*	Sapindaceae	6419.2, 6419.4
Canthium cf. *inerme*	Rubiaceae	6419.3
Commiphora cf. *marlothii*	Burseraceae	6419.1
Diospyros cf. *villosa*	Ebenaceae	6419.5
5WA-DBK, grass bedding Plan 3, BP 6384		
unidentified vitrified fragment	unidentified	6384.1

Table S9.
Rock types of lithic knapped pieces over 2 cm in layer 5WA-DBK.

	Quartzite	Hornfels	Rhyolite	Basalt	Indeterminate	TOTAL
Flake	0	17	2	1	3	**23**
Blade	4	7	1	0	2	**14**
Chunk	0	2	0	0	1	**3**
TOTAL	**4**	**26**	**3**	**1**	**6**	**40**

Table S10.
Lithic knapped pieces under 2 cm (chips/debris) in layer 5WA-DBK.

	Rhyolite/Hornfels/Quartzite/Basalt	Opaline/Agate	TOTAL
Plan 3	144	8	**152**
Plan 2	123	5	**128**
Plan 1	112	4	**116**
TOTAL	**379**	**17**	**396**

Table S11.
Occurrence of coloured microagglomerates (MA) in different sediment samples.

Provenance	Sediment nature	Block / décapage	Weight (g)	MA <150µm	MA >150µm	Number of MA per gram
Reddish Grey John	Archaeological	-	3,85	11	34	11,69
5WA-DBK	Archaeological	Block 1, décapage 1	0,97	34	111	149,48
5WA-DBK	Archaeological	Block 1, décapage 2	2,47	11	23	13,77
5WA-DBK	Archaeological	Block 1, décapage 3	2,8	8	38	16,43
5WA-DBK	Archaeological	Block 1, décapage 4	1,55	9	44	34,19
5WA-VPBK	Archaeological	-	2,05	12	0	5,85
Brown Lad	Archaeological	-	3,05	12	0	3,93
Experimental tray	Control	-	3,29	7	0	2,13

Table S12.
Coloured microagglomerate (MA) length variation in µm.

Layer	Number of pieces	Minimum	Maximum	Mean	SD	SE
Reddish Grey John	10	732	1760	1146	313	99
5WA-DBK	95	153	2976	783	476	49
5WA-VPBK	12	324	1505	665	360	104
Brown Lad	12	295	815	483	156	45
Control sediment	7	312	946	489	221	84

Table S13.
Colour and morphology of microagglomerates from archaeological layers and sediment deposited naturally inside the cave*.

Colour	Morphology	Layers					Total
		Reddish Grey John	5WA-DBK	5WA-VPBK	Brown Lad	Control sediment	
Yellow	Irregular	0	2	0	0	0	2
	Rounded	0	6	0	0	0	6
Orange	Angular	0	3	0	0	0	3
	Irregular	4	13	5	0	0	23
	Rounded	0	20	1	1	0	22
Red	Angular	0	2	0	0	0	2
	Irregular	3	7	1	0	0	11
	Rounded	0	10	0	0	0	10
Dark red	Angular	0	1	0	2	0	3
	Irregular	0	4	2	1	5	12
	Rounded	2	7	3	3	2	17
Brown	Angular	0	2	0	0	0	2
	Irregular	0	5	0	1	0	6
	Rounded	1	7	0	4	0	12
Dark brown	Irregular	0	2	0	0	0	2
	Rounded	0	4	0	0	0	4
Total		10	95	12	12	7	137

* Microagglomerates smaller than 150 μm are not considered

Table S14.
Summarised results of SEM-EDS analyses conducted on coloured microagglomerates, a possible ochre fragment and a roof spall.

Prov.	Sample type	Num.	SEM observations and EDS analysis			
			Clay-sized particles (<4µm)		Silt and sand-sized particles (>4µm)	
			Shape	Composition*	Shape	Composition*
RGJ	MA	43	Aggl	Fe *(iron oxide)*	Aggl	Si *(silicate)*
			Aggl	Ca *(carbonate)*	Irr	Cl, Na *(sodium chloride)*
RGJ	MA	44	Aggl	Fe *(iron oxide)*	Aggl	Si *(silicate)*
			Aggl	Si, Al, Ca, Fe, Na, K, Mg *(clay min.)*	Sub-circ	Fe, Cr *(undet oxide)*
			Aggl	Ca, P *(calcium phosphate)*	Ang	Ca, S *(calcium sulphate)*
					Irr	Cl, Na *(sodium chloride)*
DBK	MA	3	Sub-circ/ irr	Si *(silicate)*	Sub-circ/ irr	Si *(silicate)*
			Plat/aggl	Si, Na, Al, Fe, Ca, Mg, K *(clay min)*	Ang	Fe, Ti *(undet oxide)*
					Irr	Si, Al, K, Mg, Ca, Na, Ti *(feldspar)*
					Sub-circ	Ca, P *(calcium phosphate)*
DBK	MA	7	Aggl	Cl, Na *(sodium chloride)*	Irr	Si *(silicate)*
			Aggl	Si, Al, K, Ca, Na, Mg *(clay min)*	Ang	Fe, Ti *(undet oxide)*
					Plat	Si, K, Al, Ti, Na, Ca, Mg *(mica)*
DBK	MA	10	Aggl	Si, Al, K, Mg, Ca, Na *(clay min)*	Ang	Fe *(iron oxide)*
					Irr	Fe, Ti *(undet oxide)*
					Plat/Aggl	Si, K, Al, Na, Ti *(mica + silicates)*
DBK	MA	28	Aggl/irr	Fe *(iron oxide)*	Ang	Si *(silicate)*
			Aggl	Si, Na, Al, Fe *(mixture of iron oxides and clay min)*	Ang	Fe, Ti *(undet oxide)*
					Irr	Cl, Na *(sodium chloride)*
					Fib	C *(vegetal fibre)*
VPBK	MA	38	Ang	Si *(silicate)*	Ang/irr	Si *(silicate)*
			Aggl	Fe *(iron oxide)*	Plat	Si, Al, K *(mica)*
			Aggl	Si, K, Al *(clay min)*		
BL	MA	42	Irr	Si, K, Al, Na, Ca, Mg *(feldspar)*	Ang/irr	Si *(silicate)*
			Aggl	Fe (iron oxide)	Irr	Ca, P *(calcium phosphate)*
			Aggl	Si, Al, Fe, K, Na, Ca, P, Mg *(clay min)*		
CS	MA	39	Sub-circ	Ca, S *(calcium sulphate)*	Ang/irr	Si (silicate)
			Aggl	Ca *(carbonate)*	Plat	Fe, Cr *(undet oxide)*
					Plat	Si, Al, K, Na, Mg *(mica)*
					Ang	Ca, P *(calcium phosphate)*
					Irr	Cl, Na *(sodium chloride)*

CS	MA	40	Irr	Si (*silicate*)	Aggl	Si *(silicate)*
			Aggl	Fe (*iron oxide*)	Plat	Fe, Cr *(undet oxide)*
					Irr	Ca (*carbonate*)
					irr	Cl, Na (*sodium chloride*)
DBK	Possible ochre frag	OF1	Aggl	Si, Fe, Al, K, Na, Ca, P, Mg, Ce, Zr, La, Nd, Ti *(Mixture of iron oxides, silicates and aluminosilicates)*	Ang	Si *(silicate)*
					Ang	Fe, Ti *(undet oxide)*
					Acic	Ba, S *(barium sulphate)*
					Plat	Si, Ca, Al, K, Mg *(mica)*
					Ang	Zr, Si *(zirconium silicate)*
					Ang	Ca, P *(calcium phosphate)*
					Irr	Cl, Na *(sodium chloride)*
Control sediment	Roof spall	RS1	Aggl	Si, Al, K, Na, Fe, Ca, Ti, Mg, S *(Mixture of iron oxides, silicates and aluminosilicates)*	Ang/sub-circ	Si *(silicate)*
			Aggl/plat	Fe *(iron oxide)*	Oct	Fe, Ti (*undet oxide*)
			Aggl	Ca, S *(calcium sulphate)*	Irr	Cl, Na *(sodium chloride)*

Prov: provenance; RGJ: Reddish Grey John; DBK: Dark Brown Kevin; VPBK: Very Pale Brown Kim; BL: Brown Lad; CS: control sediment; MA: microagglomerate; frag: fragment; num: number; subcirc: subcircular; irr: irregular; ang: angular; plat: platy; aggl: agglomerate; acic: acicular; oct: octahedral.

* Interpretation in brackets.

Table S15.
Summarised results of µ-Raman analyses conducted on coloured microagglomerates, a possible ochre fragment and a roof spall.

Prov	Sam type	Num	ab	cal	flu	gth	gp	hem	kln	mag	man	ms	qz	rt	C
RGJ	MA	43				•	•	•							•
	MA	44				•	•	•	•				•		•
DBK	MA	3	•	•		•		•	•				•		•
	MA	7				•		•		•	•	•	•	•	
	MA	10						•	•	•		•		•	
	MA	28				•		•					•		
VPBK	MA	38	•	•	•		•	•					•		
BL	MA	42	•					•					•		
CS	MA	39						•					•		
	MA	40				•		•					•		
DBK	Poss ochre frag	OF1				•		•					•		
CS	Roof spall	RS1		•		•		•							

Prov: provenance; sam: sample; RGJ: Reddish Grey John; DBK: Dark Brown Kevin; VPBK: Very Pale Brown Kim; BL: Brown Lad; CS: control sediment; MA: microagglomerate; poss: possible; frag: fragment; num: number; C: Carbon. Abbreviations of minerals are based on the nomenclature suggested by (*96*), except for fluorapatite (flu), and manganite (man).

Table S16.

Table S1

Results of SEM-EDS analyses conducted on coloured microagglomerates, a possible ochre fragment and a roof spall.

Prov	Sam type	Sam num	Num of an	Description of analysed item				Semi-quantitative EDX analyses **				Interpretation***
				Grain morph	BSE cont*	Length range (µm)	Width range (µm)	>10%	10-3%	3-1%	<1%	
RGI	Microaggl	43	4	Aggl	G	-	-	**Si** (Al)	(Fe, Cl, Na, K, Mg)	(Ca, P)	(S, Ti, Mn)	Silicate (−iron ox+aluminosil)
		43	1	Aggl	W	Submicr	Submic	**Fe** (Si, Al)	(Na)	(K, Mg, Ca, Ti)	(Cl, P, Mn, S)	Iron ox (−silicates+aluminosil)
		43	2	Aggl	LG	Submicr	Submic	Ca (Cl, Si, Na)	(P, Mg)	(Al, Fe, S)	(K)	Carbonate (+iron ox- aluminosil)
		43	1	Irr	G	72	29,6	**Cl, Na**	-	(Si)	(Fe, Ca, Al, Mg)	Sodium chloride (−iron ox+silicates)
RGI	Microaggl	44	2	Irr/subcirc	LG	15,9–18,8	11,2–15,6	**Si** (Al)	(Fe, Ca, P, S)	(K, Mg, Cl)	(Ti)	Silicate (+calcium sulfates−aluminosil)
		44	1	Subcirc	W	5,6	3,6	**Fe** (S, Ca) Cr	(Ni)	Ti, Mn (Na)	(Al, Cl, K, P)	Undet ox (+calcium sulfate−aluminosil)
		44	1	Aggl	W	Submicr	Submic	(Si) Fe (Al)	(Ca, K, P, Na)	(Mg) Ti (S, Cl)	-	Iron ox (+clay min)
		44	1	Aggl	LG	Submicr	Submic	**Si**, Al, Ca	Fe, Na (S, P)	K, Mg	(Cl) Ti	Clay min (iron ox)
		44	2	Ang	LG	180,8 193,9	151,2 159	**Ca**, S	-	(Si, Fe, P, Cl, Al)	(Na, K, Mg)	Calcium sulfate (+aluminosil)
		44	2	Aggl	G	Submicr	Submic	Ca, P (Si)	(S, Fe, Al, Cl, Na, Mg)	(K)	(Ti)	Calcium phosphate (+iron ox+aluminosil)
		44	1	Irr	G	14,8	10,6	**Cl, Na**	-	(Ca, Si)	(P, Al, Fe, Mg, K, S)	Sodium chloride (+iron ox+silicates)
DBK	Microaggl	3	2	Subcirc/irr	G	1,4–2,9	1–2,9	**Si**	(Al, Cl, P, Fe, Na)	(K, Mg)	(S)	Silicate (−iron ox+aluminosil)
		3	3	Subcirc/irr	G	6,4–45,6	4–39,17	**Si**	(Fe)	(Cl, K, Mg)	(Ca, Ti, P)	Silicate (−iron ox+aluminosil)
		3	1	Ang	W	11,8	10	**Fe**, Ti (Si)	(Al)	(Mg)	(K, Na, Cl, Ca, V) Mn	Undet ox (+aluminosil)
		3	1	Irr	G	45,6	39,17	**Si**, Al (Fe)	(Cl) K, Mg	Ca, Na	Ti (P)	Feldspar (−iron ox+aluminosil)
		3	4	Plat/aggl	G	2,6–3,9	1,3–2,5	(Cl) Si, Na, Al	Fe, Ca, (P)	Mg, K	(Ti, S)	Clay min (−iron ox+sodium chloride)
		3	1	Subcirc	G	5,9	5	**Ca**, P	(Si, Fe, Cl, Al)	(Na, S, Mg, K)	(Ti)	Calcium phosphate (+iron ox+aluminosil)
DBK	Microaggl	7	2	Irr	G	12,2–20,1	9–15,7	Si (Fe)	(Al, K, Ti)	(Cl, Na)	(Mg, Na, P)	Silicate (−iron ox+aluminosil)
		7	1	Ang	W	14	8,2	**Fe** (Si)	(Al)	l, K, Ca) Ti (Na, Mg,	Mn	Iron ox (+clay min)
		7	1	Plat	G	12,7	5	**Si**, K, Al	(Fe)	Ti, Na, Ca	(Cl) Mg	Mica (+iron ox)
		7	1	Aggl	G	Submicr	Submic	**Cl**, Na (Si)	(Fe)	(Al, Ca, K)	(Ti, Mg, P)	Sodium chloride (−iron ox)

		10	1	Ang	W	4,1	2,9	**Fe** (Si)	(Al)	(K, Na) Ti (Ca, Mg, Cl)	(P)	Iron ox (+clay min + silicates)
DBK	Microaggl	10	3	Irr	W	6,3–9,9	3,1–5,2	**Fe**, Ti (Si)	(Al)	(Na, Zr, K)	(Mg, Cl, Ca) Mn (Nb, P)	Undet ox (+clay min + silicates)
		10	1	Plat	G	17,5	8,9	**Si**, K, Al	-	(Fe) Na	Ti (Cl)	Mica (+clay min + silicates)
		28	3	Ang	G	11–30,9	7,2–24,2	Si (Al)	(Cl, Fe)	(Na, K, Ca, Mg)	(Ti, P)	Silicate (+iron ox+aluminosil)
		28	3	Aggl/irr	W	Submicr–2,8	Submicr–2,2	(Si) Fe (Al)	(Cl, Na)	(Ca, Mg, K)	Ti (P)	Iron ox (+aluminosil)
DBK	Microaggl	28	1	Ang	W	143,9	100,7	Ti, Fe (Si)	(Al)	-	(Na, Ca, Mg, Cl, K, P) Mn	Undet ox (+aluminosil)
		28	2	Aggl	G	Submicr	Subcmir	(Ca), Si (Cl, P)	Na, Al, Fe	Mg, K	S, Ti	Mixture of iron ox and clay min
		28	1	Irr	LG	21,6	11,7	**Cl**, Na	(Si)	(Al)	(Fe, Ca, Mg, K)	Sodium chloride (+aluminosil)
		28	1	Fib	G	22,2	6,5	**C** (Ca, Cl, Si, Na)	(Mg, P, Al)	(K, Fe)	(S)	Vegetal fibre (+iron ox)
		38	1	Ang	G	3,6	3,5	**Si**	(Fe, Al, K, Ca)	(P, Na, Cl)	(Ti, Mg)	Silicate (+calcium phosphate+iron ox)
		38	5	Ang/irr	G	16,1–169,8	11,8–137,4	**Si**	(Ca, Cl, Al, P, Fe, Na)	(K)	(Mg, Ti, Mn, S)	Silicate (+calcium phosphate+iron ox)
VPBK	Microaggl	38	2	Aggl	W	Submicr	Subcmir	**Fe**	(Al)	(Na, K, Cl) Ti	(Ca, P, Mg)	Iron ox (+aluminosil)
		38	1	Plat	G	6,7	4,2	**Si**, Al, K	Na	(Fe) Ca	-	K-rich mica (+silicates+iron ox)
		38	1	Aggl	G	Submicr	Subcmir	**Si**, K, Al	-	Fe	Na, Cl, P, Mg	clay min (+silicates)
		42	3	Ang/irr	G	4,3–12,1	1,1–8,8	**Si** (Fe)	(Al, Ca, K, P)	(Na, Mg, Cl)	(Ti, S)	Silicate (+iron ox+aluminosil)
		42	1	Aggl	W	Submicr	Subcmir	**Fe** (Si)	(Al, Ca)	(Ti, P, Na, Mg, K)	(Cl)	Iron ox (+aluminosil)
BL	Microaggl	42	1	Irr	G	28,8	21	**Si**, K, Al	Na (Fe)	Ca (P)	Mg (Cl)	Feldspar (+iron ox)
		42	1	Aggl	G	Submicr	Subcmir	**Si**, Al, Fe	K, Na, Ca	P (Cl) Mg	(Ti)	clay min (+silicates)
		42	1	Irr	G	4,4	2,7	**Ca**, P (Si)	(Cl)	(Fe, Al, Na, S, Mg, K)	-	Calcium phosphate (+silicates+iron ox)
		39	8	Ang/irr	G	6,2–55,4	4,1–42,5	**Si** (Fe, Al)	(Cl, Ca)	(P, Na, Mg, S, K)	(Mn, Ti, Cr)	Silicate (+iron ox+aluminosil)
		39	1	Plat	W	5,9	3,6	**Fe**, Cr (Si, Ni)	-	(Mo, Mn, Al)	(Ca, Cl)	Undet ox (+aluminosil)
		39	1	Plat	G	8,8	4,6	**Si**, Al, K	(Fe), Na	Ca	(Cl) Mg	Mica (+silicates)
CS	Microaggl	39	1	Subcirc	G	2,7	2,1	Ca (Si) S	(Fe, Al)	(Cl, K, P, Na, Mg)	(Ti)	Calcium sulfate (+silicates+iron ox)
		39	1	Aggl	G	Submicr	Subcmir	**Ca** (Si)	(Fe, Al, Cl)	(Na, K, Mg)	P (Ti, S)	Carbonate (+silicates+iron ox)
		39	1	Ang	G	8	7,4	Ca, P (Si)	(Fe, Al, Mg)	(Cl, Na, S)	(K, Mn)	Calcium phosphate (+silicates+iron ox)
		39	1	Irr	G	56	43	**Cl, Na**	-	-	(Si, Fe, Ca, S, Al)	Sodium chloride (+aluminosil)

CS	Microaggl	40	7	Irr	G	1,8–4	1,6–4,5	**Si** (Fe, Al)	(Ca)	(Cl, Mg, S, K)	(S, Na, Ti)	Silicate (+iron ox+aluminosil)
		40	2	Aggl	G	-	-	**Si** (Al, Fe)	-	(Cl, K, Ca, Mg)	(P, Ti)	Silicate (+iron ox+aluminosil)
		40	1	Plat	W	5,2	2,7	Fe (Si) Cr	(Ni, Al)	(Mo, Mn)	(Na, Ca, Mg, Cl, K, P, Ti)	Undet ox (+aluminosil)
		40	1	Aggl	W	Submicr	Subcmir	**Fe (Si)**	(Al)	(Ti, Na)	(Cl, Ca, K, Mg, Mn)	Iron ox (+silicates)
		40	1	Irr	G	4,9	3,3	**Ca (Si)**	(Al, Cl, Na)	(K, S, Mg)	(Ti, P)	Carbonate (+silicates+iron ox)
		40	1	Irr	G	21,1	19,9	**Cl, Na**	-	-	(Fe, Si)	Sodium chloride (+iron ox+silicates)
DBK	Possible ochre frag	OF1	2	Ang	G	262,1–287,4	183,9–222,5	**Si** (Al)	(Na, Ca)	(K, Fe)	(Cl)	Silicate (+aluminosil)
		OF1	1	Ang	W	428,3	302	**Fe**, Ti	(Si)	(Al)	(Mg, Na, Mn, Zn, Ca, K)	Undet ox (+aluminosil)
		OF1	2	Aggl	G	Submicr	Subcmir	**Si,** Fe, Al	K, Na, Ca	P, Mg (Cl) Ce	Zr, La, Nd, Ti	Mixture of iron ox, silicates and aluminosil
		OF1	1	Acic	W	16,3	3,9	**Ba,** S (Si)	(Al, Ca)	(Fe, Na, K)	(P, Cl)	Barium sulfate (+silicates+aluminosil)
		OF1	1	Plat	G	114,1	–	(Fe) Si, Ca (P)	Al (Ce) K, Mg	(La, Nd, Cl, Na)	-	Mica (+iron ox+calcium phosphate)
		OF1	1	Ang	W	55,9	36,6	**Zr**, Si	-	(Ca, Fe)	(Al, K)	Zirconium silicate (+aluminosil)
		OF1	1	Ang	LG	55,2	42	**Ca**, P	(Fe, Si)	(Na, Fe, Cl, Ce)	(Al, K, Mg)	Calcium phosphate (+aluminosil)
		OF1	3	Irr	G	20,1–146,1	16,1–101,5	**Cl**, Na	(Si)	-	(Ca, Al. Fe, K, Mg, P, S)	Sodium chloride (+iron ox+silicates)
CS	Roof spall	RS1	5	Ang/subcirc	G	8,8–272,2	8,5–228,2	**Si**	(Al, Fe)	(K, Na, Cl)	(Ca, Mg, Ti, S, Zr, Mn)	Silicate (+iron ox+aluminosil)
		RS1	6	Aggl	LG	Submicr	Subcmir	**Si,** Al	K, Na, Fe	Ca (Cl)	Ti, Mg, S	Mixture of silicates and aluminosil
		RS1	2	Aggl	W	Submicr	Subcmir	**Fe** (Si)	(Na, Al, Cl)	K	(Mg, Ca) Ti, Mn (P, S)	Iron ox (+clay min+silicates)
		RS1	2	Plat	W	1,9–3,4	0,5–1,3	**Fe** (Si)	(Al, Na)	(K) Ti (Ca, Cl, Mg)	Mn (P)	Iron ox (+clay min+silicates)
		RS1	1	Oct	W	113,7	103,7	**Fe**, Ti	(Si, Al)	(Na, Zr, K)	(Mg, Cl, Ca, Mn, P)	Undet ox (+aluminosil)
		RS1	1	Aggl	G	Submicr	Subcmir	**Ca**, S (Si)	(Fe)	(Al, Cl, K)	(Mg, Na, P)	Calcium sulfate (+aluminosil)
		RS1	1	Irr	LG	128,5	162	**Cl**, Na	(Si)	(Al)	(Ca, Fe, Mg, K, S, P)	Sodium chloride (+aluminosil)

Prov: provenance; sam: sample; an: analyses; morph: morphology; cont: contrast; RGJ: Reddish Grey John; DBK: Dark Brown Kevin; VPBK: Very Pale Brown Kim; BL: Brown Lad; CS: control sediment; microaggl: microagglomerate; frag: fragment; subcirc: subcircular; irr: irregular; ang: angular; plat: platy; aggl: agglomerate; fib: fibrous; acic: acicular; oct: octahedral; G: grey; W: white; LG: light grey; submicr: submicrometric; ox: oxide; aluminosil: aluminosilicates; undet: undetermined; min: minerals.

* BSE cont. refers to the contrast observed on backscattered electron (BSE) images.

** Elements in brackets play no role in the mineralogical composition of the analyzed items, elements in bold are present in a proportion equal or higher than 40 %.

*** Text in brackets indicates the interpretation of detected elements surrounding the analysed area.

Table S17.
Detailed results of µ-Raman analyses conducted on coloured microagglomerates, a possible ochre fragment, and a roof spall.

Prov	Sample type	Sample num	Num of an	Morph	Colour	Identified compounds*
RGJ	MA	43	4	Aggl	R	Hem
		43	1	Platy	G	Hem (gp, C)
		43	1	Aggl	G	Hem (gp)
		43	1	Irr	B	Hem (gp)
		43	1	Aggl	G	Hem (gth)
		43	1	Subcirc	B	C
RGJ	MA	44	1	Subcirc	R	Hem
		44	1	Subcirc	BR	Hem (kln)
		44	1	Ang	R	Hem (qz)
		44	2	Aggl	O/B	Gth
		44	2	Ang/aggl	T/W	Gp (hem)
		44	2	Subcirc/aggl	B	C
		44	1	Irr	B	C (qz)
DBK	MA	3	3	Subcirc	B	Hem
		3	2	Ang	DR	Hem
		3	2	Ang	G	Hem
		3	1	Aggl	R	Hem
		3	1	Subcirc	B	Hem (kln, qz)
		3	1	Ang	DR	Hem (gth)
		3	1	Subcirc	Y	Gth (ab, cal)
		3	1	Subcirc	G	Ab
		3	1	Irr	DR	Ab
		3	1	Ang	B	C
DBK	MA	7	1	Subcirc	B	Mag
		7	1	Ang	B	Mag, rt (ms, gth)
		7	1	Subcirc	B	Man (hem)
		7	2	Irr	W	Qz (hem)
DBK	MA	10	3	Subcirc	R	Hem
		10	3	Aggl	O	Hem
		10	1	Subcirc	B	Mag, rt (hem, ms)
		10	1	Subcirc	B	Rt (hem, kln)
DBK	MA	28	1	Ang	B	Hem
		28	2	Ang	DR/B	Hem (gth)
		28	1	Subcirc	B	Hem (gth)
		28	1	Ang	Y	Gth
		28	1	Ang	DR/T	Qz, hem
		28	1	Subcirc	T	Qz (hem, gth)
VPBK	MA	38	1	Irr	B	Hem (flu)

		38	1	Irr	DR	Hem (ab)
		38	1	Aggl	O	Hem (ab, qz)
		38	2	Irr	B	Hem (ab, gp, cal)
BL	MA	42	1	Subcirc	B	Hem
		42	1	Subcirc	B	Hem (ab)
		42	1	Ang	T	Qz
CS	MA	39	1	Ang	B	Hem
		39	1	Subcirc	B	Hem (qz)
		39	1	Irr	DR/T	Qz (hem)
CS	MA	40	2	Ang	Y/BR	Gth
		40	1	Subcirc	B	Gth (hem, qz)
		40	1	Subcirc	DR/T	Qz (gth)
DBK	Possible ochre frag	OF1	1	Aggl	R	Hem
		OF1	2	Irr	B	Gth (qz)
		OF1	1	Ang	B	Gth
		OF1	1	Ang	T	Qz (gth)
		OF1	1	Ang	DR /T	Qz
CS	Roof spall	RS1	2	Aggl	R	Hem
		RS1	1	Ang	DR	Hem
		RS1	1	Subcirc	Y	Gth (hem)
		RS1	1	Subcirc	R/T	Cal

Prov: provenance; RGJ: Reddish Grey John; DBK: Dark Brown Kevin; VPBK: Very Pale Brown Kim; BL: Brown Lad; CS: control sediment; MA: microagglomerate; frag: fragment; num: number; an: analyses; morph: morphology; sub-circ: sub-circular; ang: angular; aggl: agglomerate; irr: irregular; B: black; DR: dark red; G: grey; R. red; Y: yellow; W: white; O: orange; T: translucent; BR: brown. Abbreviations of minerals are based on the nomenclature suggested by (*96*), except for fluorapatite (flu) and manganite (man). C: Carbon.

* Minerals between brackets come from grains surrounding the analysed grain.

References and Notes

1. F. Berna, P. Goldberg, L. K. Horwitz, J. Brink, S. Holt, M. Bamford, M. Chazan, Microstratigraphic evidence of in situ fire in the Acheulean strata of Wonderwerk Cave, Northern Cape province, South Africa. *Proc. Natl. Acad. Sci. U.S.A.* **109**, E1215–E1220 (2012). doi:10.1073/pnas.1117620109 Medline

2. S. Hlubik, F. Berna, C. Feibel, D. Braun, J. W. K. Harris, Researching the Nature of Fire at 1.5 Mya on the Site of FxJj20 AB, Koobi Fora, Kenya, Using High-Resolution Spatial Analysis and FTIR Spectrometry. *Curr. Anthropol.* **58**, S243–S257 (2017). doi:10.1086/692530

3. M. J. Walker, D. Anesin, D. E. Angelucci, A. Avilés-Fernández, F. Berna, A. T. Buitrago-López, Y. Fernández-Jalvo, M. Haber-Uriarte, A. López-Jiménez, M. López-Martínez, I. Martín-Lerma, J. Ortega-Rodrigáñez, J.-L. Polo-Camacho, S. E. Rhodes, D. Richter, T. Rodríguez-Estrella, J.-L. Schwenninger, A. R. Skinner, Combustion at the late Early Pleistocene site of Cueva Negra del Estrecho del Río Quípar (Murcia, Spain). *Antiquity* **90**, 571–589 (2016). doi:10.15184/aqy.2016.91

4. N. Goren-Inbar, N. Alperson, M. E. Kislev, O. Simchoni, Y. Melamed, A. Ben-Nun, E. Werker, Evidence of hominin control of fire at Gesher Benot Ya'aqov, Israel. *Science* **304**, 725–727 (2004). doi:10.1126/science.1095443 Medline

5. W. Roebroeks, P. Villa, On the earliest evidence for habitual use of fire in Europe. *Proc. Natl. Acad. Sci. U.S.A.* **108**, 5209–5214 (2011). doi:10.1073/pnas.1018116108 Medline

6. R. Shimelmitz, S. L. Kuhn, A. J. Jelinek, A. Ronen, A. E. Clark, M. Weinstein-Evron, 'Fire at will': The emergence of habitual fire use 350,000 years ago. *J. Hum. Evol.* **77**, 196–203 (2014). doi:10.1016/j.jhevol.2014.07.005 Medline

7. R. Barkai, J. Rosell, R. Blasco, A. Gopher, Fire for a Reason: Barbecue at Middle Pleistocene Qesem Cave, Israel. *Curr. Anthropol.* **58**, S314–S328 (2017). doi:10.1086/691211

8. P. Vidal-Matutano, R. Blasco, P. Sañudo, J. Fernández Peris, The Anthropogenic Use of Firewood During the European Middle Pleistocene: Charcoal Evidence from Levels XIII and XI of Bolomor Cave, Eastern Iberia (230–160 ka). *Environ. Archaeol.* **24**, 269–284 (2019). doi:10.1080/14614103.2017.1406026

9. L. Wadley, C. Sievers, M. Bamford, P. Goldberg, F. Berna, C. Miller, Middle Stone Age bedding construction and settlement patterns at Sibudu, South Africa. *Science* **334**, 1388–1391 (2011). doi:10.1126/science.1213317 Medline

10. A. M. Rosen, in *Neanderthals in the Levant: Behavioral Organization and the Beginnings of Human Modernity*, D. O. Henry, Ed. (Continuum, 2003), pp. 156–171.

11. D. Nadel, E. Weiss, O. Simchoni, A. Tsatskin, A. Danin, M. Kislev, Stone Age hut in Israel yields world's oldest evidence of bedding. *Proc. Natl. Acad. Sci. U.S.A.* **101**, 6821–6826 (2004). doi:10.1073/pnas.0308557101 Medline

12. D. Cabanes, C. Mallol, I. Expósito, J. Baena, Phytolith evidence for hearths and beds in the late Mousterian occupations of Esquilleu cave (Cantabria, Spain). *J. Archaeol. Sci.* **37**, 2947–2957 (2010). doi:10.1016/j.jas.2010.07.010

13. L. R. Backwell, F. d'Errico, W. E. Banks, P. de la Peña, C. Sievers, D. Stratford, S. J. Lennox, M. Wojcieszak, E. M. Bordy, J. Bradfield, L. Wadley, New excavations at Border Cave, KwaZulu-Natal, South Africa. *J. Field Archaeol.* **43**, 417–436 (2018). doi:10.1080/00934690.2018.1504544

14. L. Wadley, L. Backwell, F. d'Errico, C. Sievers, Cooked starchy rhizomes in Africa 170 thousand years ago. *Science* **367**, 87–91 (2020). doi:10.1126/science.aaz5926 Medline

15. P. B. Beaumont, thesis, University of Cape Town, South Africa (1978).

16. Materials and methods are available as supplementary materials.

17. R. Grün, P. Beaumont, P. V. Tobias, S. Eggins, On the age of Border Cave 5 human mandible. *J. Hum. Evol.* **45**, 155–167 (2003). doi:10.1016/S0047-2484(03)00102-7 Medline

18. A. R. Millard, Bayesian analysis of ESR dates, with application to Border Cave. *Quat. Geochronol.* **1**, 159–166 (2006). doi:10.1016/j.quageo.2006.03.002

19. S. Schiegl, P. Goldberg, O. Bar-Yosef, S. Weiner, Ash Deposits in Hayonim and Kebara Caves, Israel: Macroscopic, Microscopic and Mineralogical Observations, and their Archaeological Implications. *J. Archaeol. Sci.* **23**, 763–781 (1996). doi:10.1006/jasc.1996.0071

20. M. G. Canti, Aspects of the chemical and microscopic characteristics of plant ashes found in archaeological soils. *Catena* **54**, 339–361 (2003). doi:10.1016/S0341-8162(03)00127-9

21. H. J. Beentje, The Genus Tarchonanthus (Compositae-Mutisieae). *Kew Bull.* **54**, 81–95 (1999). doi:10.2307/4111025

22. P. Goldberg, C. E. Miller, S. Schiegl, B. Ligouis, F. Berna, N. J. Conard, L. Wadley, Bedding, hearths, and site maintenance in the Middle Stone Age of Sibudu Cave, KwaZulu-Natal, South Africa. *Archaeol. Anthropol. Sci.* **1**, 95–122 (2009). doi:10.1007/s12520-009-0008-1

23. S. M. Mentzer, Microarchaeological Approaches to the Identification and Interpretation of Combustion Features in Prehistoric Archaeological Sites. *J. Archaeol. Method Theory* **21**, 616–668 (2014). doi:10.1007/s10816-012-9163-2

24. S. Schiegl, P. W. Stockhammer, C. Scott, L. Wadley, A mineralogical and phytolith study of the Middle Stone Age hearths in Sibudu Cave, KwaZulu-Natal, South Africa : Sibudu Cave. *S. Afr. J. Sci.* **100**, 185–194 (2004).

25. R. M. Albert, S. Weiner, O. Bar-Yosef, L. Meignen, Phytoliths in the Middle Palaeolithic Deposits of Kebara Cave, Mt Carmel, Israel: Study of the Plant Materials used for Fuel and Other Purposes. *J. Archaeol. Sci.* **27**, 931–947 (2000). doi:10.1006/jasc.2000.0507

26. P. Karkanas, O. Bar-Yosef, P. Goldberg, S. Weiner, Diagenesis in Prehistoric Caves: The Use of Minerals that Form In Situ to Assess the Completeness of the Archaeological Record. *J. Archaeol. Sci.* **27**, 915–929 (2000). doi:10.1006/jasc.1999.0506

27. G. Zając, J. Szyszlak-Bargłowicz, W. Gołębiowski, M. Szczepanik, Chemical Characteristics of Biomass Ashes. *Energies* **11**, 2885 (2018). doi:10.3390/en11112885

28. T. Hakbijl, The Traditional, Historical and Prehistoric Use of Ashes as an Insecticide, with an Experimental Study on the Insecticidal Efficacy of Washed Ash. *Environ. Archaeol.* **7**, 13–22 (2002). doi:10.1179/env.2002.7.1.13

29. I. Watts, thesis, University of London (1998).

30. A. S. Brooks, J. E. Yellen, R. Potts, A. K. Behrensmeyer, A. L. Deino, D. E. Leslie, S. H. Ambrose, J. R. Ferguson, F. d'Errico, A. M. Zipkin, S. Whittaker, J. Post, E. G. Veatch, K. Foecke, J. B. Clark, Long-distance stone transport and pigment use in the earliest Middle Stone Age. *Science* **360**, 90–94 (2018). doi:10.1126/science.aao2646 Medline

31. P. W. Wiessner, Embers of society: Firelight talk among the Ju/'hoansi Bushmen. *Proc. Natl. Acad. Sci. U.S.A.* **111**, 14027–14035 (2014). doi:10.1073/pnas.1404212111 Medline

32. C. Mallol, A. Henry, Ethnoarchaeology of Paleolithic Fire: Methodological Considerations. *Curr. Anthropol.* **58**, S217–S229 (2017). doi:10.1086/691422

33. F. d'Errico, W. E. Banks, D. L. Warren, G. Sgubin, K. van Niekerk, C. Henshilwood, A.-L. Daniau, M. F. Sánchez Goñi, Identifying early modern human ecological niche expansions and associated cultural dynamics in the South African Middle Stone Age. *Proc. Natl. Acad. Sci. U.S.A.* **114**, 7869–7876 (2017). doi:10.1073/pnas.1620752114 Medline

34. L. Sitzia, E. M. Gayo, M. Sepulveda, J. S. González, L. Ibañez, A. Queffelec, R. De Pol-Holz, A perched, high-elevation wetland complex in the Atacama Desert (northern Chile) and its implications for past human settlement. *Quat. Res.* **92**, 33–52 (2019). doi:10.1017/qua.2018.144

35. O. Katz, D. Cabanes, S. Weiner, A. M. Maeir, E. Boaretto, R. Shahack-Gross, Rapid phytolith extraction for analysis of phytolith concentrations and assemblages during an excavation: An application at Tell es-Safi/Gath, Israel. *J. Archaeol. Sci.* **37**, 1557–1563 (2010). doi:10.1016/j.jas.2010.01.016

36. C. E. Cordova, C3 Poaceae and Restionaceae phytoliths as potential proxies for reconstructing winter rainfall in South Africa. *Quat. Int.* **287**, 121–140 (2013). doi:10.1016/j.quaint.2012.04.022

37. C. E. Cordova, L. Scott, in *African Palaeoenvironments and Geomorphic Landscape Evolution*, J. Runge, Ed. (Taylor and Francis, 2010), pp. 107–134.

38. I. Esteban, J. H. J. Vlok, E. L. Kotina, M. K. Bamford, R. M. Cowling, D. Cabanes, R. M. Albert, Phytoliths in plants from the south coast of the Greater Cape Floristic Region (South Africa). *Rev. Palaeobot. Palynol.* **245**, 69–84 (2017). doi:10.1016/j.revpalbo.2017.05.001

39. M. L. Murungi, "Phytoliths at Sibudu (South Africa): Implications for Vegetation, Climate and Human Occupation During the MSA," thesis, University of the Witwatersrand, South Africa (2017).

40. A. Novello, M. K. Bamford, Y. Van Wijk, S. Wurz, Phytoliths in modern plants and soils from Klasies River, Cape Region (South Africa). *Quat. Int.* **464**, 440–459 (2018). doi:10.1016/j.quaint.2017.10.009

41. L. Rossouw, “The Application of Fossil Grass-phytolith Analysis in the Reconstruction of Late Cainozoic Environments in the South African Interior,” thesis, University of the Free State, South Africa (2009).

42. I. Esteban, J. C. De Vynck, E. Singels, J. H. J. Vlok, C. W. Marean, R. M. Cowling, E. C. Fisher, D. Cabanes, R. M. Albert, Modern soil phytolith assemblages used as proxies for Paleoscape reconstruction on the south coast of South Africa. *Quat. Int.* **434**, 160–179 (2017). doi:10.1016/j.quaint.2016.01.037

43. International Committee for Phytolith Taxonomy (ICPT), International code for phytolith nomenclature (ICPN) 2.0. *Ann. Bot.* **124**, 189–199 (2019). doi:10.1093/aob/mcz064 Medline

44. R. D. Drennan, in *Statistics for Archaeologists: A Common Sense Approach* (Springer, ed. 2, 2009), pp. 97–104.

45. Ø. Hammer, *PAST Palaeontological Statistics Version 3.23 Reference Manual* (Natural History Museum, Univ. of Oslo, 2019).

46. Ø. Hammer, D. A. T. Harper, P. D. Ryan, PAST: Palaeontological Statistics software package for education and data analysis. *Palaeontol. Electron.* **4**, 4 (2001); https://palaeo-electronica.org/2001_1/past/issue1_01.htm.

47. E. A. Wheeler, InsideWood - a web resource for hardwood anatomy. *IAWA J.* **32**, 199–211 (2011). doi:10.1163/22941932-90000051

48. E. A. Wheeler, P. Baas, P. E. Gasson, IAWA list of microscopic features for hardwood identification. *IAWA Bull.* **10**, 219–232 (1989). doi:10.1163/22941932-90000496

49. C. P. Kromhout, *'N Sleutel vir die Mikroskopiese Uitkenning van die Vernaamste Inheemse Houtsoorte van Suid-Afrika* (Staatsdrukker, 1975).

50. J. Ilic, *CSIRO Atlas of Hardwoods* (Crawford House Press, 1991).

51. K. Neumann, W. Schoch, P. Détienne, F. H. Schweingruber, *Woods of the Sahara and the Sahel: An Anatomical Atlas* (Haupt, 2000).

52. L. F. Allott, “Palaeoenvironments of the Middle Stone Age at Sibudu Cave, KwaZulu-Natal, South Africa: an Analysis of Archaeological Charcoal,” thesis, University of the Witwatersrand, South Africa (2005).

53. J. Chikumbirike, “Archaeological and Palaeoecological Implications of Charcoal Assemblages Dated to the Holocene from Great Zimbabwe and its Hinterland,” thesis, University of the Witwatersrand, South Africa (2014).

54. S. J. Lennox, “Woody Taxa from Charcoal in Sibudu’s Middle Stone Age Hearths,” thesis, University of the Witwatersrand, South Africa (2016).

55. R. Scheel-Ybert, Charcoal collections of the world. *IAWA J.* **37**, 489–505 (2016). doi:10.1163/22941932-20160148

56. E. Asouti, C. Kabukcu, Holocene semi-arid oak woodlands in the Irano-Anatolian region of southwest Asia: Natural or anthropogenic? *Quat. Sci. Rev.* **90**, 158–182 (2014). doi:10.1016/j.quascirev.2014.03.001

57. E. Dotte-Sarout, X. Carah, C. Byrne, Not just carbon: Assessment and prospects for the application of anthracology in Oceania. *Archaeol. Ocean.* **50**, 1–22 (2015). doi:10.1002/arco.5041

58. A. Höhn, S. Kahlheber, K. Neumann, A. Schweizer, in *Dynamics of Forest Ecosystems in Central Africa During the Holocene: Past–Present–Future*, J. Runge, Ed. (Taylor and Francis, 2008), pp. 29–41.

59. W. Hubau, J. Van den Bulcke, K. Bostoen, B. Olivier Clist, A. Livingstone Smith, N. Defoirdt, F. Mees, L. Nsenga, J. Van Acker, H. Beeckman, Archaeological charcoals as archives for firewood preferences and vegetation composition during the late Holocene in the southern Mayumbe, Democratic Republic of the Congo (DRC). *Veg. Hist. Archaeobot.* **23**, 591–606 (2014). doi:10.1007/s00334-013-0415-1

60. W. Hubau, J. Van den Bulcke, P. Kitin, L. Brabant, J. Van Acker, H. Beeckman, Complementary imaging techniques for charcoal examination and identification. *IAWA J.* **34**, 147–168 (2013). doi:10.1163/22941932-00000013

61. W. Hubau, J. van den Bulcke, P. Kitin, F. Mees, J. Van Acker, H. Beeckman, Charcoal identification in species-rich biomes: A protocol for Central Africa optimised for the Mayumbe forest. *Rev. Palaeobot. Palynol.* **171**, 164–178 (2012). doi:10.1016/j.revpalbo.2011.11.002

62. O. Nelle, V. Robin, B. Talon, Pedoanthracology: Analysing soil charcoal to study Holocene palaeoenvironments. *Quat. Int.* **289**, 1–4 (2013). doi:10.1016/j.quaint.2012.11.024

63. R. Scheel-Ybert, M. Beauclair, A. Buarque, The Forest People: Landscape and firewood use in the Araruama region, southeastern Brazil, during the late Holocene. *Veg. Hist. Archaeobot.* **23**, 97–111 (2014). doi:10.1007/s00334-013-0397-z

64. M. K. Bamford, Late Pliocene woody vegetation of Area 41, Koobi Fora, East Turkana Basin, Kenya. *Rev. Palaeobot. Palynol.* **164**, 191–210 (2011). doi:10.1016/j.revpalbo.2011.01.004

65. M. K. Bamford, Macrobotanical remains from Wonderwerk Cave (Excavation 1). Oldowan to Late Pleistocene (2 Ma to 14 ka BP), South Africa. *Afr. Archaeol. Rev.* **32**, 813–838 (2015). doi:10.1007/s10437-015-9200-0

66. M. K. Bamford, in *Changing Climates, Ecosystems and Environments within Arid Southern Africa and Adjoining Regions: Palaeoecology of Africa 33*, J. Runge, Ed. (Taylor and Francis, 2015), pp. 153–174.

67. P. de la Peña, Refining our understanding of Howiesons Poort lithic technology: The evidence from Grey Rocky layer in Sibudu Cave (KwaZulu-Natal, South Africa). *PLOS ONE* **10**, e0143451 (2015). doi:10.1371/journal.pone.0143451 Medline

68. B. Lafuente, R. T. Downs, H. Yang, N. Stone, in *Highlights in Mineralogical Crystallography*, T. Armbruster, R. M. Danisi, Eds. (De Gruyter, 2015), pp. 1–30.

69. L. G. Benning, V. R. Phoenix, N. Yee, M. J. Tobin, Molecular characterization of cyanobacterial silicification using synchrotron infrared micro-spectroscopy. *Geochim. Cosmochim. Acta* **68**, 729–741 (2004). doi:10.1016/S0016-7037(03)00489-7

70. C. Genestar, C. Pons, Earth pigments in painting: Characterisation and differentiation by means of FTIR spectroscopy and SEM-EDS microanalysis. *Anal. Bioanal. Chem.* **382**, 269–274 (2005). doi:10.1007/s00216-005-3085-8 Medline

71. L.-M. Shillito, M. J. Almond, J. Nicholson, M. Pantos, W. Matthews, Rapid characterisation of archaeological midden components using FT-IR spectroscopy, SEM-EDX and micro-XRD. *Spectrochim. Acta A Mol. Biomol. Spectrosc.* **73**, 133–139 (2009). doi:10.1016/j.saa.2009.02.004 Medline

72. C. M. Müller, B. Pejcic, L. Esteban, C. Delle Piane, M. Raven, B. Mizaikoff, Infrared attenuated total reflectance spectroscopy: An innovative strategy for analyzing mineral components in energy relevant systems. *Sci. Rep.* **4**, 6764 (2014). doi:10.1038/srep06764 Medline

73. D. Bikiaris, Daniilia Sister, S. Sotiropoulou, O. Katsimbiri, E. Pavlidou, A. P. Moutsatsou, Y. Chryssoulakis, Ochre-differentiation through micro-Raman and micro-FTIR spectroscopies: Application on wall paintings at Meteora and Mount Athos, Greece. *Spectrochim. Acta A Mol. Biomol. Spectrosc.* **56**, 3–18 (2000). doi:10.1016/S1386-1425(99)00134-1 Medline

74. S. Schiegl, N. Conard, The Middle Stone Age sediments at Sibudu: Results from FTIR spectroscopy and microscopic analyses. *South. Afr. Humanit.* **18**, 149–172 (2006).

75. S. Yoshioka, Y. Kitano, Transformation of aragonite to calcite through heating. *Geochem. J.* **19**, 245–249 (1985). doi:10.2343/geochemj.19.245

76. C. Lancelotti, J. Ruiz-Pérez, J. J. García-Granero, Investigating fuel and fireplaces with a combination of phytoliths and multi-element analysis, an ethnographic experiment. *Veg. Hist. Archaeobot.* **26**, 75–83 (2017). doi:10.1007/s00334-016-0574-y

77. R. M. Albert, O. Lavi, L. Estroff, S. Weiner, A. Tsatskin, A. Ronen, S. Lev-Yadun, Mode of occupation of Tabun Cave, Mt Carmel, Israel, during the Mousterian Period: A study of the sediments and phytoliths. *J. Archaeol. Sci.* **26**, 1249–1260 (1999). doi:10.1006/jasc.1999.0355

78. R. M. Albert, S. Weiner, in *Phytoliths: Applications in Earth Sciences and Human History*, J. D. Meunier, F. Colin, Eds. (Taylor and Francis, 2001), pp. 251–266.

79. R. M. Albert, R. Shahack-Gross, D. Cabanes, A. Gilboa, S. Lev-Yadun, M. Portillo, I. Sharon, E. Boaretto, S. Weiner, Phytolith-rich layers from the Late Bronze and Iron Ages at Tel Dor (Israel): Mode of formation and archaeological significance. *J. Archaeol. Sci.* **35**, 57–75 (2008). doi:10.1016/j.jas.2007.02.015

80. G. Tsartsidou, P. Karkanas, G. Marshall, N. Kyparissi-Apostolika, Palaeoenvironmental reconstruction and flora exploitation at the Palaeolithic cave of Theopetra, central Greece: The evidence from phytolith analysis. *Archaeol. Anthropol. Sci.* **7**, 169–185 (2015). doi:10.1007/s12520-014-0183-6

81. I. Esteban, "Reconstructing past vegetation and modern human foraging strategies on the south coast of South Africa," thesis, Universitat de Barcelona (2016).

82. J. M. Watt, M. G. Breyer-Brandwijk, *The Medicinal and Poisonous Plants of Southern and Eastern Africa* (Livingstone, 1962).

83. F. d'Errico, L. Backwell, P. Villa, I. Degano, J. J. Lucejko, M. K. Bamford, T. F. Higham, M. P. Colombini, P. B. Beaumont, Early evidence of San material culture represented by organic artifacts from Border Cave, South Africa. *Proc. Natl. Acad. Sci. U.S.A.* **109**, 13214–13219 (2012). doi:10.1073/pnas.1204213109 Medline

84. P. Villa, S. Soriano, T. Tsanova, I. Degano, T. F. G. Higham, F. d'Errico, L. Backwell, J. J. Lucejko, M. P. Colombini, P. B. Beaumont, Border Cave and the beginning of the Later Stone Age in South Africa. *Proc. Natl. Acad. Sci. U.S.A.* **109**, 13208–13213 (2012). doi:10.1073/pnas.1202629109 Medline

85. M. I. Bird, L. K. Fifield, G. M. Santos, P. B. Beaumont, Y. Zhou, M. L. Di Tada, P. A. Hausladen, Radiocarbon dating from 40–60 ka BP at Border Cave, South Africa. *Quat. Sci. Rev.* **22**, 943–947 (2003). doi:10.1016/S0277-3791(03)00005-2

86. R. Grün, P. Beaumont, Border Cave revisited: A revised ESR chronology. *J. Hum. Evol.* **40**, 467–482 (2001). doi:10.1006/jhev.2001.0471 Medline

87. R. M. Albert, C. W. Marean, The exploitation of plant resources by early *Homo sapiens*: The phytolith record from Pinnacle Point 13B Cave, South Africa. *Geoarchaeol.* **27**, 363–384 (2012). doi:10.1002/gea.21413

88. I. Esteban, C. W. Marean, E. C. Fisher, P. Karkanas, D. Cabanes, R. M. Albert, Phytoliths as an indicator of early modern humans plant gathering strategies, fire fuel and site occupation intensity during the Middle Stone Age at Pinnacle Point 5-6 (south coast, South Africa). *PLOS ONE* **13**, e0198558 (2018). doi:10.1371/journal.pone.0198558 Medline

89. P. de la Peña, A. Val, D. J. Stratford, F. Colino, I. Esteban, J. M. Fitchett, T. Hodgskiss, J. Matembo, R. Moll, Revisiting Mwulu's Cave: New insights into the Middle Stone Age in the southern African savanna biome. *Archaeol. Anthropol. Sci.* **11**, 3239–3266 (2019). doi:10.1007/s12520-018-0749-9

90. I. Esteban, R. M. Albert, A. Eixea, J. Zilhão, V. Villaverde, Neanderthal use of plants and past vegetation reconstruction at the Middle Paleolithic site of Abrigo de la Quebrada (Chelva, Valencia, Spain). *Archaeol. Anthropol. Sci.* **9**, 265–278 (2017). doi:10.1007/s12520-015-0279-7

91. V. Villaverde, C. Real, D. Roman, R. M. Albert, E. Badal, M. Á. Bel, M. M. Bergadà, P. de Oliveira, A. Eixea, I. Esteban, Á. Martínez-Alfaro, C. M. Martínez-Varea, M. Pérez-Ripoll, The early Upper Palaeolithic of Cova de les Cendres (Alicante, Spain). *Quat. Int.* **515**, 92–124 (2019). doi:10.1016/j.quaint.2017.11.051

92. M. Alonso-Eguíluz, J. Fernández-Eraso, R. M. Albert, The first herders in the upper Ebro basin at Los Husos II (Álava, Spain): Microarchaeology applied to fumier deposits. *Veg. Hist. Archaeobot.* **26**, 143–157 (2017). doi:10.1007/s00334-016-0590-y

93. M. Portillo, S. Kadowaki, Y. Nishiaki, R. M. Albert, Early Neolithic household behavior at Tell Seker al-Aheimar (Upper Khabur, Syria): A comparison to ethnoarchaeological study of phytoliths and dung spherulites. *J. Archaeol. Sci.* **42**, 107–118 (2014). doi:10.1016/j.jas.2013.10.038

94. D. Namdar, A. Zukerman, A. M. Maeir, J. C. Katz, D. Cabanes, C. Trueman, R. Shahack-Gross, S. Weiner, The 9th century BCE destruction layer at Tell es-Safi/Gath, Israel:

Integrating macro- and microarchaeology. *J. Archaeol. Sci.* **38**, 3471–3482 (2011). doi:10.1016/j.jas.2011.08.009

95. Y. Devos, C. Nicosia, L. Vrydaghs, L. Speleers, J. van der Valk, E. Marinova, B. Claes, R. M. Albert, I. Esteban, T. B. Ball, M. Court-Picon, A. Degraeve, An integrated study of Dark Earth from the alluvial valley of the Senne River (Brussels, Belgium). *Quat. Int.* **460**, 175–197 (2017). doi:10.1016/j.quaint.2016.06.025

96. D. L. Whitney, B. W. Evans, Abbreviations for names of rock-forming minerals. *Am. Mineral.* **95**, 185–187 (2010). doi:10.2138/am.2010.3371